# Measurements of azimuthal anisotropy and charged-particle multiplicity in d + Au collisions at √sNN=200, 62.4, 39, and 19.6 GeV

**Aidala, C.; ...; Dumancic, Mirta; ...; Makek, Mihael; ...; Zou, L.**

# Measurements of azimuthal anisotropy and charged-particle multiplicity in $d$ + Au collisions at $\sqrt{s_{NN}}$ = 200, 62.4, 39, and 19.6 GeV

C. Aidala,[39] Y. Akiba,[50,51,*] M. Alfred,[22] K. Aoki,[30] N. Apadula,[27] C. Ayuso,[39] V. Babintsev,[23] A. Bagoly,[16] K. N. Barish,[8] S. Bathe,[5,51] A. Bazilevsky,[7] R. Belmont,[12] A. Berdnikov,[53] Y. Berdnikov,[53] D. S. Blau,[32,42] M. Boer,[35] J. S. Bok,[44] M. L. Brooks,[35] J. Bryslawskyj,[5,8] V. Bumazhnov,[23] C. Butler,[20] S. Campbell,[13] V. Canoa Roman,[55] C. Y. Chi,[13] M. Chiu,[7] M. Connors,[20,51] M. Csanád,[16] T. Csörgő,[17,61] T. W. Danley,[45] M. S. Daugherity,[1] G. David,[7,55] K. DeBlasio,[43] K. Dehmelt,[55] A. Denisov,[23] A. Deshpande,[51,55] E. J. Desmond,[7] J. H. Do,[62] A. Drees,[55] K. A. Drees,[6] M. Dumancic,[60] J. M. Durham,[35] A. Durum,[23] T. Elder,[20] A. Enokizono,[50,52] S. Esumi,[58] B. Fadem,[40] W. Fan,[55] N. Feege,[55] D. E. Fields,[43] M. Finger,[9] M. Finger, Jr.,[9] S. L. Fokin,[32] J. E. Frantz,[45] A. Franz,[7] A. D. Frawley,[19] Y. Fukuda,[58] C. Gal,[55] P. Gallus,[14] P. Garg,[3,55] H. Ge,[55] Y. Goto,[50,51] N. Grau,[2] S. V. Greene,[59] T. Gunji,[11] T. Hachiya,[51] J. S. Haggerty,[7] K. I. Hahn,[18] S. Y. Han,[18] S. Hasegawa,[28] T. O. S. Haseler,[20] X. He,[20] T. K. Hemmick,[55] K. Hill,[12] A. Hodges,[20] K. Homma,[21] B. Hong,[31] T. Hoshino,[21] N. Hotvedt,[27] J. Huang,[7] S. Huang,[59] J. Imrek,[15] M. Inaba,[58] D. Isenhower,[1] Y. Ito,[41] D. Ivanishchev,[49] B. V. Jacak,[55] Z. Ji,[55] B. M. Johnson,[7,20] V. Jorjadze,[55] D. Jouan,[47] D. S. Jumper,[24] J. H. Kang,[62] D. Kapukchyan,[8] S. Karthas,[55] A. V. Kazantsev,[32] V. Khachatryan,[55] A. Khanzadeev,[49] C. Kim,[8,31] D. J. Kim,[29] E.-J. Kim,[10] M. Kim,[54] M. H. Kim,[31] D. Kincses,[16] E. Kistenev,[7] T. Koblesky,[12] D. Kotov,[49,53] S. Kudo,[58] K. Kurita,[52] J. G. Lajoie,[27] E. O. Lallow,[40] A. Lebedev,[27] S. H. Lee,[27,55] M. J. Leitch,[35] Y. H. Leung,[55] N. A. Lewis,[39] X. Li,[35] S. H. Lim,[35,62] L. D. Liu,[48] M. X. Liu,[35] V.-R. Loggins,[24] S. Lökös,[16,17] D. Lynch,[7] T. Majoros,[15] M. Makek,[63] M. Malaev,[49] V. I. Manko,[32] E. Mannel,[7] H. Masuda,[52] M. McCumber,[35] D. McGlinchey,[12,35] W. J. Metzger,[17] A. C. Mignerey,[38] D. E. Mihalik,[55] A. Milov,[60] D. K. Mishra,[4] J. T. Mitchell,[7] G. Mitsuka,[51] T. Moon,[62] D. P. Morrison,[7] S. I. M. Morrow,[59] T. Murakami,[33,50] J. Murata,[50,52] K. Nagai,[57] K. Nagashima,[21] T. Nagashima,[52] J. L. Nagle,[12] M. I. Nagy,[16] I. Nakagawa,[50,51] H. Nakagomi,[50,58] K. Nakano,[50,57] C. Nattrass,[56] R. Nouicer,[7,51] T. Novák,[17,61] N. Novitzky,[55] R. Novotny,[14] A. S. Nyanin,[32] E. O'Brien,[7] C. A. Ogilvie,[27] J. D. Orjuela Koop,[12] J. D. Osborn,[39] A. Oskarsson,[36] K. Ozawa,[30,58] V. Pantuev,[25] V. Papavassiliou,[44] J. S. Park,[54] S. Park,[50,54,55] S. F. Pate,[44] M. Patel,[27] W. Peng,[59] D. V. Perepelitsa,[7,12] G. D. N. Perera,[44] C. E. PerezLara,[55] R. Petti,[7] M. Phipps,[7,24] C. Pinkenburg,[7] A. Pun,[45] M. L. Purschke,[7] P. V. Radzevich,[53] K. F. Read,[46,56] V. Riabov,[42,49] Y. Riabov,[49,53] D. Richford,[5] T. Rinn,[27] M. Rosati,[27] Z. Rowan,[5] J. Runchey,[27] T. Sakaguchi,[7] H. Sako,[28] V. Samsonov,[42,49] M. Sarsour,[20] K. Sato,[58] S. Sato,[28] B. Schaefer,[59] B. K. Schmoll,[56] R. Seidl,[50,51] A. Sen,[27,56] R. Seto,[8] A. Sexton,[38] D. Sharma,[55] I. Shein,[23] T.-A. Shibata,[50,57] K. Shigaki,[21] M. Shimomura,[27,41] C. L. Silva,[35] D. Silvermyr,[36] M. J. Skoby,[39] M. Slunečka,[9] K. L. Smith,[19] R. A. Soltz,[34] S. P. Sorensen,[56] I. V. Sourikova,[7] P. W. Stankus,[46] S. P. Stoll,[7] T. Sugitate,[21] A. Sukhanov,[7] S. Syed,[20] A. Takeda,[41] K. Tanida,[28,51,54] M. J. Tannenbaum,[7] S. Tarafdar,[59,60] A. Taranenko,[42] G. Tarnai,[15] R. Tieulent,[20,37] A. Timilsina,[27] M. Tomášek,[14] C. L. Towell,[1] R. S. Towell,[1] I. Tserruya,[60] Y. Ueda,[21] B. Ujvari,[15] H. W. van Hecke,[35] S. Vazquez-Carson,[12] J. Velkovska,[59] M. Virius,[14] V. Vrba,[14,26] X. R. Wang,[44,51] Z. Wang,[5] Y. Watanabe,[50,51] C. P. Wong,[20] C. Xu,[44] Q. Xu,[59] Y. L. Yamaguchi,[51,55] A. Yanovich,[23] P. Yin,[12] J. H. Yoo,[31] I. Yoon,[54] H. Yu,[44] I. E. Yushmanov,[32] W. A. Zajc,[13] S. Zharko,[53] and L. Zou[8]

(PHENIX Collaboration)

[1]*Abilene Christian University, Abilene, Texas 79699, USA*

[2]*Department of Physics, Augustana University, Sioux Falls, South Dakota 57197, USA*

[3]*Department of Physics, Banaras Hindu University, Varanasi 221005, India*

[4]*Bhabha Atomic Research Centre, Bombay 400 085, India*

[5]*Baruch College, City University of New York, New York, New York 10010, USA*

[6]*Collider-Accelerator Department, Brookhaven National Laboratory, Upton, New York 11973-5000, USA*

[7]*Physics Department, Brookhaven National Laboratory, Upton, New York 11973-5000, USA*

[8]*University of California-Riverside, Riverside, California 92521, USA*

[9]*Charles University, Ovocný trh 5, Praha 1, 116 36, Prague, Czech Republic*

[10]*Chonbuk National University, Jeonju, 561-756, Korea*

[11]*Center for Nuclear Study, Graduate School of Science, University of Tokyo, 7-3-1 Hongo, Bunkyo, Tokyo 113-0033, Japan*

[12]*University of Colorado, Boulder, Colorado 80309, USA*

[13]*Columbia University, New York, New York 10027 and Nevis Laboratories, Irvington, New York 10533, USA*

[14]*Czech Technical University, Zikova 4, 166 36 Prague 6, Czech Republic*

[15]*Debrecen University, H-4010 Debrecen, Egyetem tér 1, Hungary*

[16]*ELTE, Eötvös Loránd University, H-1117 Budapest, Pázmány P. s. 1/A, Hungary*

[17]*Eszterházy Károly University, Károly Róbert Campus, H-3200 Gyöngyös, Mátrai út 36, Hungary*

[18]*Ewha Womans University, Seoul 120-750, Korea*

[19]*Florida State University, Tallahassee, Florida 32306, USA*

[20]*Georgia State University, Atlanta, Georgia 30303, USA*

[21]*Hiroshima University, Kagamiyama, Higashi-Hiroshima 739-8526, Japan*

[22]*Department of Physics and Astronomy, Howard University, Washington, DC 20059, USA*

[23]*IHEP Protvino, State Research Center of Russian Federation, Institute for High Energy Physics, Protvino, 142281, Russia*

[24]*University of Illinois at Urbana-Champaign, Urbana, Illinois 61801, USA*

 

[25]*Institute for Nuclear Research of the Russian Academy of Sciences, prospekt 60-letiya Oktyabrya 7a, Moscow 117312, Russia*
[26]*Institute of Physics, Academy of Sciences of the Czech Republic, Na Slovance 2, 182 21 Prague 8, Czech Republic*
[27]*Iowa State University, Ames, Iowa 50011, USA*
[28]*Advanced Science Research Center, Japan Atomic Energy Agency, 2-4 Shirakata Shirane, Tokai-mura, Naka-gun, Ibaraki-ken 319-1195, Japan*
[29]*Helsinki Institute of Physics and University of Jyväskylä, P.O.Box 35, FI-40014 Jyväskylä, Finland*
[30]*KEK, High Energy Accelerator Research Organization, Tsukuba, Ibaraki 305-0801, Japan*
[31]*Korea University, Seoul, 136-701, Korea*
[32]*National Research Center "Kurchatov Institute", Moscow, 123098, Russia*
[33]*Kyoto University, Kyoto 606-8502, Japan*
[34]*Lawrence Livermore National Laboratory, Livermore, California 94550, USA*
[35]*Los Alamos National Laboratory, Los Alamos, New Mexico 87545, USA*
[36]*Department of Physics, Lund University, Box 118, SE-221 00 Lund, Sweden*
[37]*IPNL, CNRS/IN2P3, Univ Lyon, Universit Lyon 1, F-69622, Villeurbanne, France*
[38]*University of Maryland, College Park, Maryland 20742, USA*
[39]*Department of Physics, University of Michigan, Ann Arbor, Michigan 48109-1040, USA*
[40]*Muhlenberg College, Allentown, Pennsylvania 18104-5586, USA*
[41]*Nara Women's University, Kita-uoya Nishi-machi Nara 630-8506, Japan*
[42]*National Research Nuclear University, MEPhI, Moscow Engineering Physics Institute, Moscow, 115409, Russia*
[43]*University of New Mexico, Albuquerque, New Mexico 87131, USA*
[44]*New Mexico State University, Las Cruces, New Mexico 88003, USA*
[45]*Department of Physics and Astronomy, Ohio University, Athens, Ohio 45701, USA*
[46]*Oak Ridge National Laboratory, Oak Ridge, Tennessee 37831, USA*
[47]*IPN-Orsay, Univ. Paris-Sud, CNRS/IN2P3, Université Paris-Saclay, BP1, F-91406, Orsay, France*
[48]*Peking University, Beijing 100871, People's Republic of China*
[49]*PNPI, Petersburg Nuclear Physics Institute, Gatchina, Leningrad region, 188300, Russia*
[50]*RIKEN Nishina Center for Accelerator-Based Science, Wako, Saitama 351-0198, Japan*
[51]*RIKEN BNL Research Center, Brookhaven National Laboratory, Upton, New York 11973-5000, USA*
[52]*Physics Department, Rikkyo University, 3-34-1 Nishi-Ikebukuro, Toshima, Tokyo 171-8501, Japan*
[53]*Saint Petersburg State Polytechnic University, St. Petersburg, 195251, Russia*
[54]*Department of Physics and Astronomy, Seoul National University, Seoul 151-742, Korea*
[55]*Department of Physics and Astronomy, Stony Brook University, SUNY, Stony Brook, New York 11794-3800, USA*
[56]*University of Tennessee, Knoxville, Tennessee 37996, USA*
[57]*Department of Physics, Tokyo Institute of Technology, Oh-okayama, Meguro, Tokyo 152-8551, Japan*
[58]*Tomonaga Center for the History of the Universe, University of Tsukuba, Tsukuba, Ibaraki 305, Japan*
[59]*Vanderbilt University, Nashville, Tennessee 37235, USA*
[60]*Weizmann Institute, Rehovot 76100, Israel*
[61]*Institute for Particle and Nuclear Physics, Wigner Research Centre for Physics, Hungarian Academy of Sciences (Wigner RCP, RMKI) H-1525 Budapest 114, POBox 49, Budapest, Hungary*
[62]*Yonsei University, IPAP, Seoul 120-749, Korea*
[63]*Department of Physics, Faculty of Science, University of Zagreb, Bijenička c. 32 HR-10002 Zagreb, Croatia*
(Received 24 August 2017; revised manuscript received 14 November 2017; published 26 December 2017)

We present measurements of the elliptic flow ($v_2$) as a function of transverse momentum ($p_T$), pseudorapidity ($\eta$), and centrality in $d+$Au collisions at $\sqrt{s_{NN}} = 200$, 62.4, 39, and 19.6 GeV. The beam-energy scan of $d+$Au collisions provides a testing ground for the onset of flow signatures in small collision systems. We measure a nonzero $v_2$ signal at all four collision energies, which, at midrapidity and low $p_T$, is consistent with predictions from viscous hydrodynamic models. Comparisons with calculations from parton transport models (based on the AMPT Monte Carlo generator) show good agreement with the data at midrapidity to forward ($d$-going) rapidities and low $p_T$. At backward (Au-going) rapidities and $p_T > 1.5\,\mathrm{GeV}/c$, the data diverges from AMPT calculations of $v_2$ relative to the initial geometry, indicating the possible dominance of nongeometry related correlations, referred to as nonflow. We also present measurements of the charged-particle multiplicity ($dN_{\mathrm{ch}}/d\eta$) as a function of $\eta$ in central $d+$Au collisions at the same energies. We find that in $d+$Au collisions at $\sqrt{s_{NN}} = 200$ GeV the $v_2$ scales with $dN_{\mathrm{ch}}/d\eta$ over all $\eta$ in the PHENIX acceptance. At $\sqrt{s_{NN}} = 62.4$, and 39 GeV, $v_2$ scales with $dN_{\mathrm{ch}}/d\eta$ at midrapidity and forward rapidity, but falls off at backward rapidity. This

*akiba@rcf.rhic.bnl.gov

departure from the $dN_{\rm ch}/d\eta$ scaling may be a further indication of nonflow effects dominating at backward rapidity.

DOI: 10.1103/PhysRevC.96.064905

## I. INTRODUCTION

Measurements of the azimuthal momentum anisotropy of particles produced in high-energy heavy ion collisions ($A + A$) have provided strong evidence for the formation of a strongly coupled quark-gluon plasma (QGP) [1–4]. This anisotropy, as measured by the Fourier coefficients, $v_n$, can be understood as arising from initial geometry propagated to final-state momentum correlations via interactions between medium constituents. These interactions have been well described by relativistic hydrodynamics with a low ratio of viscosity to entropy density [5,6].

In 2012, measurements of $v_2$ in $\sqrt{s_{NN}} = 5.02$ TeV $p + $Pb collisions at the Large Hadron Collider (LHC) [7–9] and $\sqrt{s_{NN}} = 200$ GeV $d + $Au collisions at the Relativistic Heavy Ion Collider (RHIC) [10] raised the question whether a QGP might be formed even in these small collision systems. Further measurements in $p + $Pb collisions revealed that the signal persists for multiparticle correlations [11–14], which is additional evidence of collective behavior. To test the signal's connection to the initial geometry of the collision, PHENIX measured $v_2$ in $p/d/^3$He + Au collisions and $v_3$ in $^3$He + Au collisions at $\sqrt{s_{NN}} = 200$ GeV [15–18]. The results are consistent with the interpretation that the measured $v_2$ arises from initial geometry. High-multiplicity $p + p$ collisions at $\sqrt{s_{NN}} = 2.76$, 5.02, 7.13, and 13 TeV exhibit similar effects [19–21] and may also be related to the initial geometry [22].

Even in these small collision systems, the data at both RHIC and the LHC can be described by hydrodynamic calculations [17,22]. However, it has also been shown that calculations using kinetic theories of hadronic and partonic scattering (e.g., a multiphase transport (AMPT) model [23]) can qualitatively describe the $v_2$ measured in small systems [17,24,25]. In both hydrodynamic and kinetic models, initial geometry (coordinate space anisotropy) is translated to final state momentum space anisotropy via interactions between medium constituents. In contrast, other explanations, including color recombination [26] and initial-state effects from glasma diagrams [27], have also been proposed, where the final-state momentum correlations are due to initial momentum correlations rather than a connection to the initial geometry.

Throughout this paper we use a working definition of "flow" as initial geometry propagated to final-state azimuthal momentum anisotropy, regardless of the mechanism of propagation (e.g., fluid flow or particle transport). All other sources of final-state azimuthal momentum anisotropy are referred to as "nonflow." Examples of nonflow include jet correlations, resonance decays, and Coulomb interactions.

In 2016, RHIC delivered $d + $Au collisions at $\sqrt{s_{NN}} =$ 200, 62.4, 39, and 19.6 GeV to investigate the onset of collectivity. PHENIX has previously published results on multiparticle correlations from this data set [28], providing evidence for collective behavior at all energies. Here we report comprehensive measurements of $v_2$ as a function of $p_T$, $\eta$, and centrality in $d + $Au collisions at $\sqrt{s_{NN}} = 200$, 62.4, 39, and 19.6 GeV. We also report measurements of the charged particle multiplicity ($dN_{\rm ch}/d\eta$) as a function of $\eta$ in central $d + $Au collisions at the same energies.

## II. EXPERIMENT AND DATA SET

The PHENIX detector is described in detail in Ref. [29] and shown schematically in Fig. 1. Global event characterization and triggering use two beam-beam counters (BBC) [30] located in the pseudorapidity region $3.1 < |\eta| < 3.9$, as well as a forward silicon vertex detector (FVTX) [31] covering $1 < |\eta| < 3$. Each BBC comprises 64 Čerenkov counters arrayed around the beam pipe 1.44 m from the nominal interaction region. The counters comprise 3 cm of quartz coupled to a mesh-dynode photomultiplier tube, where the charge is calibrated to a minimum-ionizing charged particle. The FVTX is made up of two annular endcaps, each with four stations of silicon mini-strip sensors. Each station comprises 47 individual silicon sensors, each of which contains two columns of mini-strips with 75 $\mu$m pitch in the radial direction and lengths in the $\phi$ direction varying from 3.4 mm at the inner radius to 11.5 mm at the outer radius. The negative-rapidity *south*-side region (Au-going direction) has the BBCS and FVTXS arms, while the positive-rapidity *north*-side region ($d$-going direction) has the BBCN and FVTXN arms. Charged-particle tracking is provided by the *east* and *west* central arms at midrapidity, covering $|\eta| < 0.35$ each with an azimuthal ($\phi$) coverage of $\pi/2$.

At 200 and 62.4 GeV a minimum bias (MB) interaction trigger is provided by the BBC. For the MB trigger, at least one hit tube is required in each of the north and south detectors. The fraction of the $d + $Au inelastic cross section that the MB trigger fires on, $\epsilon_{\rm MB}$, is given in Table I for both energies. In addition to the MB trigger, a high-multiplicity trigger that required >40 (29) hit tubes in the BBCS for 200 (62.4) GeV was also run, providing a factor of 188 (11) enhancement of high-multiplicity events. Analyzed events were further required to have a reconstructed collision vertex in the longitudinal direction as reconstructed by the BBC of $|z_{\rm vrtx}| < 10$ cm. The resulting number of analyzed events is shown in Table I.

At 39 and 19.6 GeV, the FVTX combined with the south BBC is used for the MB trigger. This combination has a larger trigger efficiency at these lower energies than a BBC coincidence due to the low multiplicities in the region $3.1 < \eta < 3.9$ at these energies. The FVTX trigger requires at least one hit in 3 of the 4 stations of the FVTX in a given sector covering approximately $\Delta\phi = 0.26$ rad, effectively requiring a single track in each of the north and south arms. To reduce background, at least one hit tube was required in the south BBC. The efficiency of the MB trigger, $\epsilon_{\rm MB}$ at both energies is given in Table I. Additionally, a high-multiplicity trigger

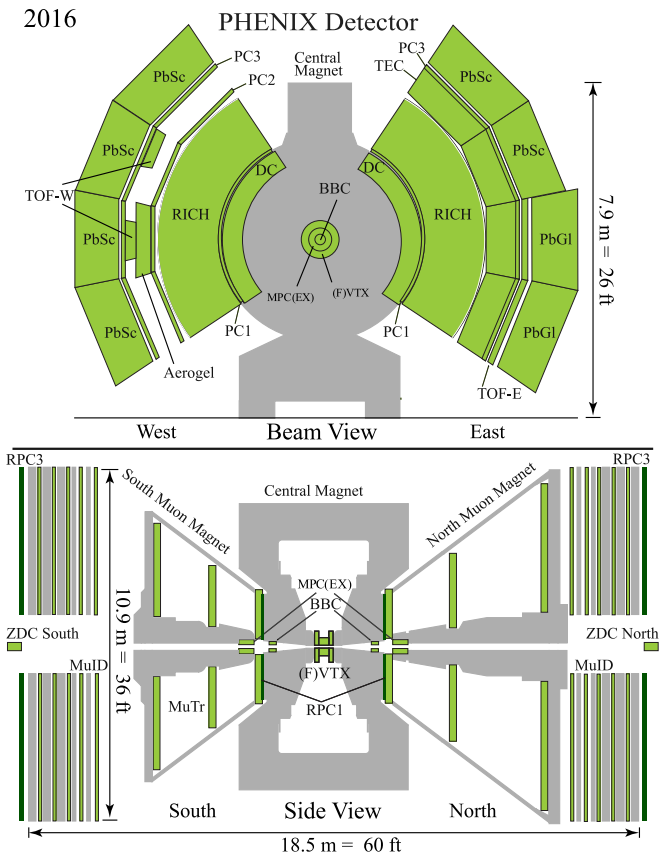


FIG. 1. A schematic view of the PHENIX detector as configured in 2016.

was implemented that further required >27 (18) hits in the south BBC for 39 (19.6) GeV, providing a factor of 6.0 (1.8) enhancement of high-multiplicity events. Analyzed events were also required to have $|z_{\rm vrtx}| < 10$ cm, as reconstructed by the FVTX. To reduce beam-gas and beam-pipe background, the total number of reconstructed clusters in the FVTX, both south and north arms, was required to be <500 (300) at 39 (19.6) GeV. The resulting number of analyzed events is shown in Table I.

The collision centrality at all four energies is determined using the total charge in the south (Au-going) BBC, as described in Ref. [32]. Figure 2 shows the BBCS charge distributions from MB triggered data at each energy along with the limits of

TABLE I. Summary of the data analyzed by PHENIX from the 2016 RHIC $d$ + Au beam energy scan.

| $\sqrt{s_{NN}}$ [GeV] | $\epsilon_{\rm MB}$ | No. analyzed MB triggered events [$10^6$] | No. analyzed high-multiplicity triggered events [$10^6$] |
|---|---|---|---|
| 200 | 88 ± 4% | 53 | 569 (0%–5%) |
| 62.4 | 78 ± 4% | 113 | 214 (0%–10%) |
| 39 | 74 ± 6% | 231 | 171 (0%–20%) |
| 19.6 | 61 ± 8% | 33 | 7 (0%–20%) |

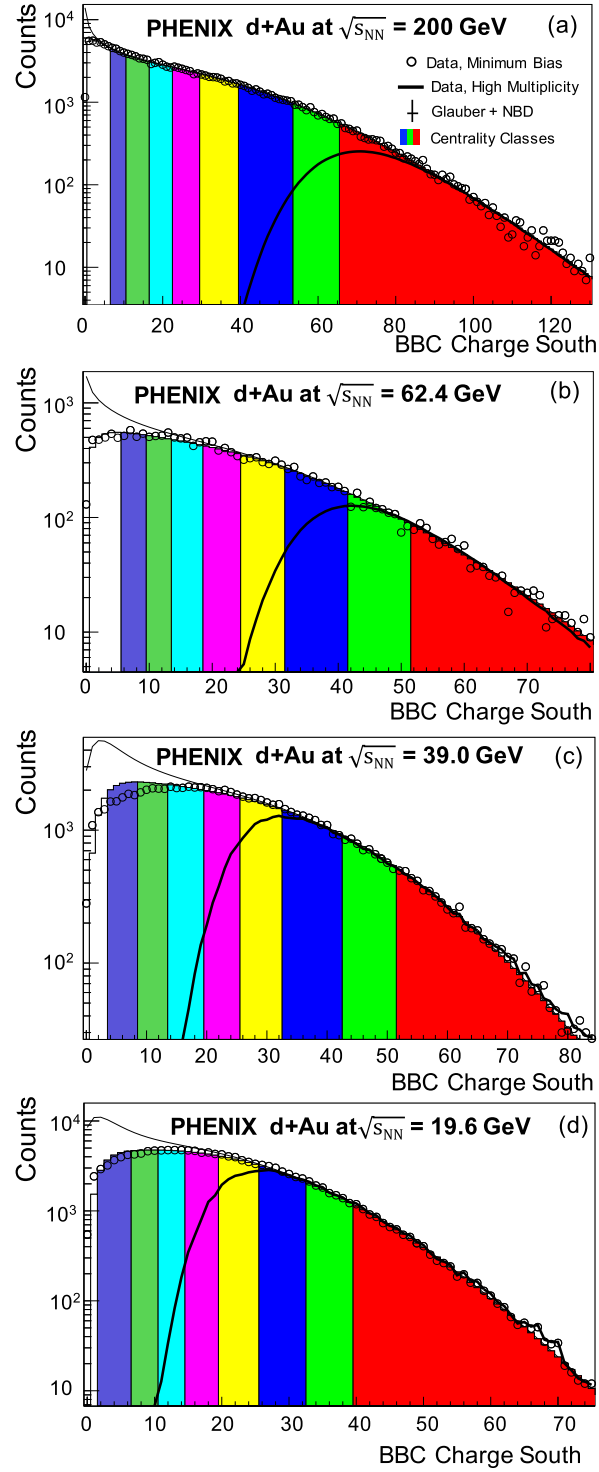


FIG. 2. The distributions of total charge in the BBCS for $d$ + Au collisions at $\sqrt{s_{NN}} = 200$ (a), 62.4 (b), 39 (c), and 19.6 (d) GeV. The data is from MB collisions, and we note that, as discussed in the text, the MB trigger definition changes with energy. The colored bands represent, from right to left, the centrality categorizations 0%–5%, 5%–10%, 10%–15%, 15%–20%, 20%–30%, 30%–40%, 40%–50%, 50%–60%, and 60%–XX%, where XX is the value of the MB trigger efficiency for each energy, given in Table I. The thick solid line shows the high-multiplicity trigger selection, scaled down to match the MB distribution.

TABLE II. Summary of the mean number of participants, $\langle N_{\rm part}\rangle$, and eccentricity, $\langle\varepsilon_2\rangle$, for central $d+$Au collisions at $\sqrt{s_{NN}} = 200$, 62.4, 39, and 19.6 GeV.

| $\sqrt{s_{NN}}$ [GeV] | Centrality | $\langle N_{\rm part}\rangle$ | $\langle\varepsilon_2\rangle$ |
|---|---|---|---|
| 200 | 0%–5% | $17.8 \pm 1.2$ | $0.54 \pm 0.04$ |
| 62.4 | 0%–5% | $16.3 \pm 1.0$ | $0.55 \pm 0.05$ |
| 39 | 0%–10% | $15.9 \pm 1.0$ | $0.56 \pm 0.06$ |
| 19.6 | 0%–20% | $13.6 \pm 1.0$ | $0.55 \pm 0.05$ |

the various centrality bins. It also includes the BBCS charge distributions for the high-multiplicity trigger, renormalized to match the high-charge region, showing the trigger turn-on at each energy. To avoid bias in the centrality distribution, analyzed events firing the high-multiplicity trigger are required to have centrality 0%–5%, 0%–10%, 0%–20%, 0%–20% at $\sqrt{s_{NN}} = 200$, 62.4, 39, and 19.6, respectively. These regions correspond to centralities for which the high-multiplicity trigger was efficient.

Using Monte Carlo–Glauber combined with fluctuations modeled by a negative binomial distribution as laid out in Ref. [32], the mean number of participants, $\langle N_{\rm part}\rangle$, and the mean initial geometry eccentricity, $\langle\varepsilon_2\rangle$, can be characterized for given centrality bins. Table II shows the $\langle N_{\rm part}\rangle$ and $\langle\varepsilon_2\rangle$ values for central collisions at all four energies. The $\langle\varepsilon_2\rangle$ values are consistent at all four collision energies within uncertainties. The $\langle N_{\rm part}\rangle$ values, however, decrease with decreasing energy. This can be attributed to both the decreasing nucleon-nucleon interaction cross section and the larger centrality bins at 39 and 19.6 GeV, which were used to improve the statistical precision of the measurements.

In the central arms, unidentified charged particle tracking uses the drift chamber (DC) and pad chamber (PC) layers. We require tracks to have a unique match between DC hits and PC hits in the layer immediately surrounding the DC. Tracks are further required to have a matching hit in the third PC layer at $R = 4.98$ m that is within $\pm 3\sigma$ of the projected track location, where $\sigma$ characterizes the momentum-dependent widths of the matching distributions.

In addition to triggering, the FVTX is used for unidentified charged particle tracking. The FVTX does not measure track momentum, and we therefore are limited to a momentum integrated measurement. We require reconstructed tracks in the FVTX to have hits in at least three of the four stations with fit quality, $\chi^2/\text{d.o.f.} < 5$. We further require that the distance of closest approach of the track to the primary collision vertex, $DCA$, be within 2.0 cm in both the $x$ and $y$ directions, transverse to the beam axis. The expected $DCA$ resolution from simulation is $\approx$1.2 cm at 500 MeV. This loose cut on the $DCA$ removes background from upstream beam-gas interactions, as well as misreconstructed tracks.

The luminosity delivered by RHIC for $d+$Au collisions at $\sqrt{s_{NN}} = 200$ GeV is high enough that approximately 6% of events are expected to contain multiple collisions (i.e., pile-up). The fraction of pile-up events is larger in central events, and is expected to be as large as 20% in the highest luminosity periods. An algorithm was developed to aid in rejecting these events. For each event, the distribution of times for each hit tube in the BBCS is determined. Then, the fraction, $f$, of the time distribution for that event which is within a 0.5 ns window of the mode of the measured distribution is calculated. Because multiple collisions typically occur at different positions along the beam axis, particles from these collisions tend to leave multiple peaks in the distribution of times recorded in the BBCS. Therefore, pile-up events are typically characterized by low values of $f$. We reject events with $f < 0.95$ for centrality 0%–20%. Studies using low luminosity data and manufactured pile-up events indicate that this cut rejects 81% of pile-up events while accepting 93% of single collision events for 0%–5% central collisions. Based on the luminosities delivered at 62.4, 39, and 19.6 GeV, fewer than 1% of events are expected to contain multiple collisions, and therefore no cut on $f$ is included.

## III. ANALYSIS

We first discuss two-particle correlation functions in Sec. III A. The analysis of the $p_T$ dependence of the second-order flow coefficient, $v_2$, is discussed in Sec. III B. The analysis of the $\eta$ dependence of $v_2$ is discussed in Sec. III C. The analysis of $dN_{\rm ch}/d\eta$ is discussed in Sec. III D.

### A. Two-particle correlations

We start by constructing long-range azimuthal correlations in $d+$Au collisions at $\sqrt{s_{NN}} = 200$ GeV. The two-particle correlation function is defined as

$$C(\Delta\phi) = \frac{S(\Delta\phi)}{M(\Delta\phi)} \frac{\int_0^{2\pi} M(\Delta\phi)}{\int_0^{2\pi} S(\Delta\phi)}, \quad (1)$$

where $\Delta\phi$ is the difference in the azimuthal angles between two tracks, $S(\Delta\phi)$ is the signal distribution, constructed from track pairs in the same event, and $M(\Delta\phi)$ is the mixed event distribution, constructed from track pairs from different events in the same centrality and collision vertex class. Figure 3 shows $C(\Delta\phi)$ for correlations of tracks between different detectors in central $d+$Au collisions at $\sqrt{s_{NN}} = 200$ GeV: (a) between tracks in the central arms and tracks in the FVTXS, (b) between tracks in the central arms and tubes in the BBCS, (c) between tracks in the FVTXS and FVTXN, and (d) between tubes in the BBCS and BBCN. By comparing $C(\Delta\phi)$ distributions between different sets of detectors we naturally change the $\Delta\eta$ requirement for the pair of tracks. Correlations with a small $\Delta\eta$ are typically thought to be dominated by nonflow correlations, particularly from intrajet correlations near $\Delta\phi = 0$, as well as dijet correlations near $\Delta\phi = \pi$. By increasing the $\Delta\eta$ gap between particles we naturally reduce the dominance of these nonflow correlations. Figure 3 shows correlation functions with (a) $0.65 < |\Delta\eta| < 3.35$, (b) $2.75 < |\Delta\eta| < 4.25$, (c) $2.0 < |\Delta\eta| < 6.0$, and (d) $6.2 < |\Delta\eta| < 7.8$.

The correlations exhibit two visible peaks at $\Delta\phi = 0$ and $\Delta\phi = \pi$. The peak at $\Delta\phi = \pi$ is associated with, for example, dijets. The peak at $\Delta\phi = 0$ does not arise from particles within a jet or decays, because we have imposed a large $\Delta\eta$ gap. This peak was first observed in $A+A$ collisions and has been termed the long-range near-side ridge. This near-side ridge was one of the key components in understanding the hydrodynamic description of $A+A$ collisions (See Ref. [33] and references

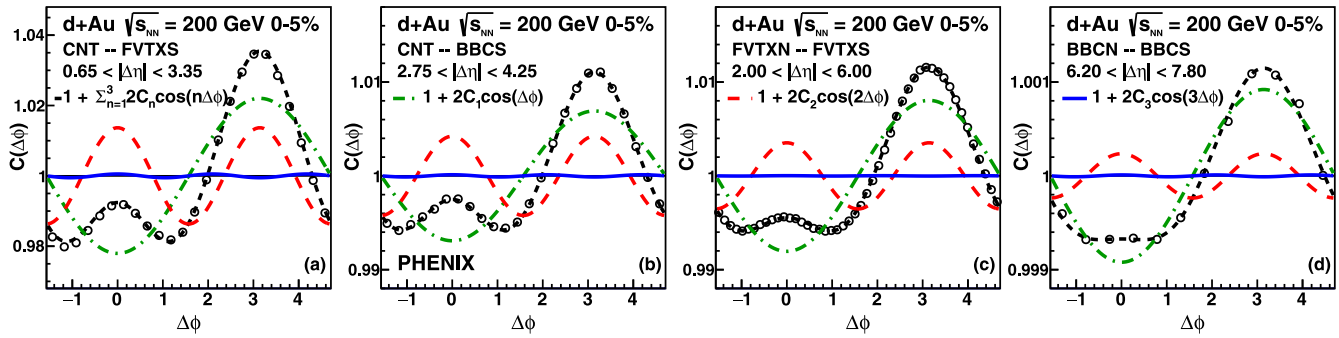


FIG. 3. Two-particle $\Delta\phi$ correlations in central $d$ + Au collisions at $\sqrt{s_{NN}} = 200$ GeV between various detectors. The blue dot-dashed lines, red long-dashed lines, and green dotted lines, correspond to the $C_1$, $C_2$, and $C_3$ components, respectively. The black dashed lines correspond to the sum of the $C_n$'s up to third order. For the correlations in panels (a) and (b), CNT tracks were required to be within $0.2 < p_T$ [GeV/$c$] $< 5.0$.

therein). The observation of this structure in high-multiplicity $p + p$ collisions at $\sqrt{s_{NN}} = 7$ TeV [20] was one of the first hints that collectivity may exist even in small collision systems. We observe a visible near-side ridge up to $|\Delta\eta| > 2.75$.

To investigate these correlations further, we fit the distribution with a Fourier series up to third order:

$$F(\Delta\phi) = 1 + \sum_{n=1}^{3} 2C_n \cos n\Delta\phi, \tag{2}$$

where $C_n$ is the $n$th order Fourier component. The full fit and the components are shown as lines in Fig. 3. The dominant term is the first-order $C_1$ term, and arises from elementary processes, such as momentum conservation. The second-order term, $C_2$, is associated with flow. While the longest range correlation shown in Fig. 3(d), with $|\Delta\eta| > 6.2$, does not show a clear peak at $\Delta\phi = 0$, it does include a strong second-order Fourier component, $C_2$.

Using the two-particle correlation (2PC) functions $C(\Delta\phi, p_T)$, the $v_2$ as a function of $p_T$, $v_2\{2PC\}$, can be calculated for central arm tracks using

$$v_2\{2PC\} = \sqrt{\frac{C^{AB}(\Delta\phi, p_T) \times C^{AC}(\Delta\phi, p_T)}{C^{BC}(\Delta\phi)}}, \tag{3}$$

where the superscript $AB$ refers to correlations between central arm and FVTXS tracks, $AC$ refers to correlations between central arm tracks and BBCS tubes, and $BC$ refers to correlations between FVTXS tracks and BBCS tubes. This relation can be understood as arising from the assumption of flow factorization, which allows the correlation function to be interpreted as, e.g., $C^{AB}(\Delta\phi) = \langle v_n^A v_n^B \rangle$. In that way, Eq. (3) reduces to

$$v_2\{2PC\} = \sqrt{\frac{\langle v_n^A v_n^B \rangle \langle v_n^A v_n^C \rangle}{\langle v_n^B v_n^C \rangle}}, \tag{4}$$

where the superscripts $A$, $B$, $C$ represent the central arms, the FVTXS, and the BBCS, respectively.

The $v_2\{2PC\}$ versus $p_T$ for 0%–5% $d$ + Au collisions at $\sqrt{s_{NN}} = 200$ GeV is shown as the red points in Fig. 4.

We also investigate the energy dependence of the near-side ridge using correlations between tracks in the FVTXN and FVTXS. Figure 5 shows $C(\Delta\phi)$ with $2.0 < |\Delta\eta| < 6.0$ for central $d$ + Au collisions at $\sqrt{s_{NN}} = 200$, 62.4, 39, and 19.6 GeV. A visible peak at $\Delta\phi = 0$ is only observed at 200 GeV; however, substantial $C_2$ components are extracted at 62.4 and 39 GeV. At 19.6 GeV, no visible $C_2$ component is extracted. The $C(\Delta\phi)$ is integrated over $p_T$ and hence dominated by low $p_T$ tracks. Therefore, the lack of a visible $C_2$ component at 19.6 GeV does not exclude a nonzero $v_2$, particularly at higher $p_T$.

### B. Analysis of $v_2$ versus $p_T$ using the event-plane method

The standard event-plane method [34] is used to calculate $v_2$ as a function of $p_T$:

$$v_2(p_T) = \frac{\langle \cos 2\left(\phi_{\rm trk}(p_T) - \Psi_2^{\rm FVTXS}\right)\rangle}{R\left(\Psi_2^{\rm FVTXS}\right)}, \tag{5}$$

where $\phi_{\rm trk}$ is the azimuthal angle of tracks in the central arms, and $\Psi_2^{\rm FVTXS}$ is the azimuthal angle of the second-

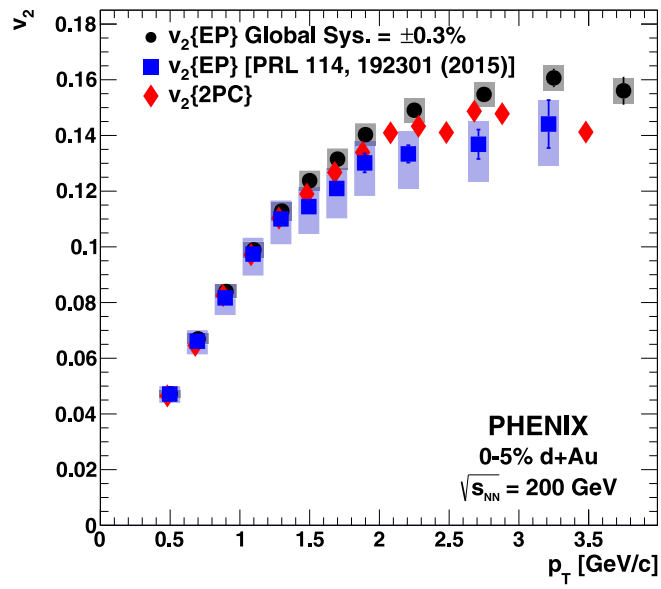


FIG. 4. The $v_2$ vs. $p_T$ in 0%–5% central $d$ + Au collisions at $\sqrt{s_{NN}} = 200$ GeV using the event-plane method (black filled circles) and two-particle correlations (red filled diamonds). Also shown are the previously published $v_2$ vs. $p_T$ using the event-plane method (blue filled squares) from PHENIX using data collected in 2008 [15].

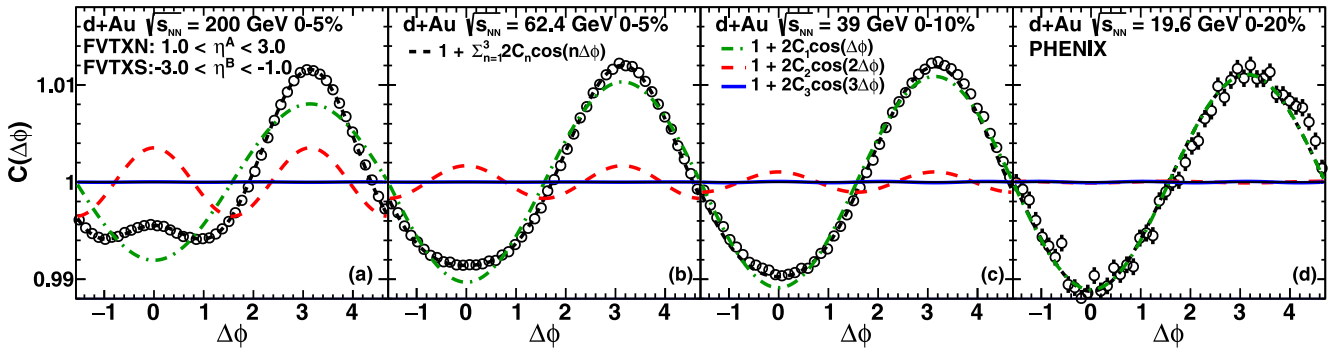


FIG. 5. Two-particle $\Delta\phi$ correlations in central $d$ + Au collisions at $\sqrt{s_{NN}} = 200$, 62.4, 39, and 19.6 GeV between tracks in the north and south FVTX detectors. The blue dot-dashed lines, red long-dashed lines, and green dotted lines, correspond to the $C_1$, $C_2$, and $C_3$ components, respectively. The black dashed lines correspond to the sum of the $C_n$'s up to third order.

order event-plane measured by the FVTXS. The event plane in the FVTXS is constructed in the usual way of $2\psi_2 = \text{atan2}(Q_y^{\text{FVTXS}}, Q_x^{\text{FVTXS}})$, with $Q^{\text{FVTXS}} = \sum_{i=1}^{M} e^{in\phi_i}$, where $\phi_i$ is the azimuthal angle of some cluster in the FVTXS. The underlying physics correlation is the same whether one uses tracks or clusters, but the use of clusters provides higher event-plane resolution and therefore greater statistical precision. The resolution of $\Psi_2^{\text{FVTXS}}$, $R(\Psi_2^{\text{FVTXS}})$, is calculated using the three-subevent method [34] that correlates measurements in the FVTXS, BBCS, and central arms. The resolution is strongly dependent on both the collision energy and centrality and is shown in Table III. We note that for 39 to 200 GeV we find that $R(\Psi_2^{\text{FVTXS}})$ increases in the most peripheral centrality bin. This is contrary to expectations, because $R(\Psi_2^{\text{FVTXS}})$ depends on both the $v_2$ in the event-plane region and the number of particles, both of which are expected to decrease in more peripheral events. Nonflow is likely the largest contribution in the most peripheral collisions and may result in this increased resolution.

TABLE III. Resolution of $\Psi_2$ measured in the BBCS and FVTXS at each energy and centrality.

| $\sqrt{s_{NN}}$ [GeV] | Centrality | $R(\Psi_2^{\text{BBCS}})$ | $R(\Psi_2^{\text{FVTXS}})$ |
|---|---|---|---|
| 200 | 0%–5% | $0.1073 \pm 0.0003$ | $0.2382 \pm 0.0007$ |
| 200 | 5%–10% | $0.085 \pm 0.004$ | $0.21 \pm 0.01$ |
| 200 | 10%–20% | $0.073 \pm 0.003$ | $0.168 \pm 0.008$ |
| 200 | 20%–40% | $0.045 \pm 0.003$ | $0.18 \pm 0.01$ |
| 200 | 40%–60% | $0.031 \pm 0.003$ | $0.17 \pm 0.02$ |
| 200 | 60%–88% | $0.133 \pm 0.003$ | $0.22 \pm 0.05$ |
| 62.4 | 0%–5% | $0.0496 \pm 0.0009$ | $0.134 \pm 0.002$ |
| 62.4 | 5%–10% | $0.0367 \pm 0.0009$ | $0.112 \pm 0.003$ |
| 62.4 | 10%–20% | $0.033 \pm 0.002$ | $0.097 \pm 0.006$ |
| 62.4 | 20%–40% | $0.026 \pm 0.001$ | $0.089 \pm 0.004$ |
| 62.4 | 40%–60% | $0.017 \pm 0.001$ | $0.091 \pm 0.006$ |
| 62.4 | 60%–78% | $0.009 \pm 0.001$ | $0.14 \pm 0.02$ |
| 39 | 0%–10% | $0.0255 \pm 0.0009$ | $0.069 \pm 0.002$ |
| 39 | 10%–20% | $0.014 \pm 0.001$ | $0.055 \pm 0.005$ |
| 39 | 20%–40% | $0.010 \pm 0.001$ | $0.055 \pm 0.008$ |
| 39 | 40%–60% | $0.008 \pm 0.002$ | $0.037 \pm 0.007$ |
| 39 | 60%–74% | $0.009 \pm 0.002$ | $0.05 \pm 0.01$ |

Due to its better resolution, we use the measurement of $\Psi_2$ from the FVTXS. However, we can compare the $v_2$ versus $p_T$ measured using the BBCS, which has a larger separation of $|\Delta\eta| > 2.75$ relative to the central arm tracks compared to $|\Delta\eta| > 0.65$ with the FVTXS. The $v_2$ values are found to agree within 2.5% for $p_T < 2\,\text{GeV}/c$, where we expect nonflow effects to be small. For $p_T > 2\,\text{GeV}/c$ a larger value of $v_2$ is observed using the FVTXS compared to the BBCS. This difference is likely due to differences in the nonflow contributions, which are expected to be larger at high $p_T$ given the smaller $\Delta\eta$ gap between the event plane and the track.

At 19.6 GeV, no combination of three-subevents yields a real valued event-plane resolution. We expect that this is due to the low multiplicity at 19.6 GeV combined with the strong $\eta$ dependence of $v_2$. We therefore extrapolate the $R(\Psi_2^{\text{FVTXS}})$ from the results at higher energies. The event-plane resolution is expected to follow the form [35]

$$R(\chi) = \frac{\sqrt{\pi}}{2}\chi e^{-\chi/2}\left[I_0\left(\frac{\chi^2}{2}\right) + I_1\left(\frac{\chi^2}{2}\right)\right], \qquad (6)$$

where $\chi = v_2\sqrt{N}$, $N$ is the multiplicity, and $I_i$ are the modified Bessel functions. The measured resolutions at 200, 62.4, and 39 GeV are used to extrapolate the resolution at 19.6 GeV under the following three assumptions:

(1) The $v_2$ is constant with $\sqrt{s_{NN}}$.
(2) The $v_2$ follows the energy dependence given by the AMPT model [23], which has been found to reasonably reproduce the energy dependence of $v_2$ in small collision systems [17,24].
(3) The $v_2$ follows the energy dependence given by AMPT for 200–39 GeV, but at 19.6 GeV the $v_2$ is the same as at 39 GeV.

Using the measured multiplicities, we find that all three assumptions give results that are in good agreement with the measured resolutions at 200–39 GeV. We take the average extrapolated resolution from the three cases and assign the maximum extent of the variation as a systematic uncertainty. This procedure gives a value of $R(\Psi_2^{\text{FVTXS}}) = 0.031^{+0.011}_{-0.016}$ for 0%–20% central collisions at $\sqrt{s_{NN}} = 19.6$ GeV.

TABLE IV. Systematic uncertainties on measurements of $v_2$ versus $p_T$.

| Source | Type | $\sqrt{s_{NN}}$ [GeV] | | | |
|---|---|---|---|---|---|
| | | 200 | 62.4 | 39 | 19.6 |
| Track Background | B | 2.0% | 2.0% | 2.0% | 2.0% |
| Event Pile-up | B | 1.0% | <1% | <1% | <1% |
| Beam Angle | B | <1%–5% | <1%–9% | <1%–8% | <1% |
| Event-Plane Detector | B | 2.5% | 2.5% | 2.5% | 2.5% |
| Event-Plane Method | B | 0.4%–17.5% | 0.4%–17.5% | 1.6%–17.5% | 6.2% |
| Event-Plane Resolution | C | 0.3%–23.0% | 1.8%–12.8% | 3.6%–20.4% | $^{+35\%}_{-48\%}$ |

During the $d+$Au data taking in 2016, a 1.0 mrad offset between the colliding beams and the longitudinal axis of PHENIX was required due to the asymmetric collision species. We negate this effect by applying a counter rotation to each central arm track, FVTX cluster, and BBC tube. After applying the counter rotation, we find no appreciable offset between the $v_2(p_T)$ measured in the east ($\pi/2 < \phi < 3\pi/2$) and west ($-\pi/2 < \phi < \pi/2$) central arms for central events. However, as we go toward more peripheral events, an increasing difference between the east and west central arms is observed. This may be due to a decrease in the flow $v_2$ signal relative to background uncorrelated to the beam axis. When calculating $\Psi_2^{\mathrm{FVTXS}}$, we use the standard $Q$ vector approach [34]. To account for any remaining beam offset or background effects, we apply a centrality and collision energy-dependent offset to the $y$ component of the 2nd order $Q$ vector, $\Delta Q_y$, such that the difference between the east and west central arms is removed.

The dominant sources of systematic uncertainty in the measurement of $v_2(p_T)$ are: (1) Track background from photon conversions and weak decays. We estimate the effect of these tracks by comparing the $v_2$ measured with a tighter cut on the matching window required for hits in the third layer of the PC. We find that this increases the $v_2$ by up to 2%, independent of centrality and energy. (2) Contamination from event pile-up. The effect of pile-up at 200 GeV is estimated by varying the pile-up rejection between $0.92 < f < 0.98$. This has a negligible effect on the $v_2$, and we assign a 1% uncertainty at 200 GeV. (3) Uncertainty on $\Delta Q_y$. As a conservative estimate, we vary the $\Delta Q_y$ values by ±50% and compare the resulting $v_2(p_T)$ values. An uncertainty of <1%–9% that varies with energy and centrality is assigned based on the study. (4) The difference between the $v_2(p_T)$ values measured independently using the FVTXS and BBCS event planes. As discussed above, this difference for $p_T < 2\,\mathrm{GeV}/c$ is found to be 2.5% independent of centrality and energy. (5) The difference between the event-plane and two-particle-correlation methods. As shown in Fig. 4, there is good agreement between the two methods in central collisions; however, there is some difference for more peripheral collisions. We include this difference as an additional systematic uncertainty. (6) Uncertainty in the event-plane resolution as given in Table III. As discussed above, the resolution at 19.6 GeV is extrapolated from the measured results at 200–39 GeV and a systematic uncertainty is assigned based on varying the assumptions of the extrapolation. The uncertainties are summarized in Table IV, categorized by *type*. PHENIX considers three categories of systematic uncertainties:

(1) Type A: point-to-point uncorrelated;
(2) Type B: point-to-point correlated;
(3) Type C: global scale uncertainties.

On all plots, type A uncertainties are represented as vertical error bars, type B uncertainties by filled boxes, and type C uncertainties are quoted on the plot or in the legend.

In previous PHENIX publications on flow in small systems [16,17], an estimation of the nonflow contributions to the measured $v_2$ has been included in the systematic uncertainties. The estimation used the ratio of the $C_2$ measured in $p+p$ collisions, scaled by the relative charge in the BBCS, to the $C_2$ measured in $p/d/^3\mathrm{He}+\mathrm{Au}$. In Ref. [15], nonflow was estimated to contribute positively between ∼5% at $p_T = 1\,\mathrm{GeV}/c$ and ∼10% at $p_T = 4\,\mathrm{GeV}/c$ to the observed $v_2$ signal. This estimation assumes that correlations in $p+p$ collisions come from nonflow alone, which may be an overestimate given recent results in $p+p$ collisions at the LHC. In this analysis we lack a suitable $p+p$ reference at all four energies and, therefore, do not make any estimation of the nonflow contributions to the measured $v_2$ in this paper.

Figure 4 shows the $v_2$ versus $p_T$ in 0%–5% central $d+$Au collisions at $\sqrt{s_{NN}} = 200$ GeV measured with the event-plane method compared to the two-particle correlation method described above. The two methods are consistent with each other. The two-particle method always gives the RMS average of $v_2$, i.e., $\sqrt{\langle v_2^2\rangle}$. By contrast, the event-plane method is an estimator of $\langle v_2^\alpha\rangle^{1/\alpha}$ [35], where $1 < \alpha < 2$. For sufficiently high-multiplicities, e.g., in central $A+A$, $\alpha$ approaches 1 and the event-plane method is an estimator of $\langle v_2\rangle$. As the multiplicity decreases, $\alpha$ approaches 2 and the event-plane method is equivalent to the two-particle method. The consistency between the two methods here demonstrates we are in the regime where the multiplicity is low enough that the two methods are equivalent. It is important to remember, then, that all event-plane method results have the same dependence on the fluctuations of the $v_2$ distribution as the two-particle method.

Also shown in Fig. 4 is the previously published measurement of $v_2(p_T)$ in 0%–5% central $d+$Au collisions at $\sqrt{s_{NN}} =$ 200 from PHENIX using data collected in 2008 [15]. The results are in good agreement for $p_T < 2\,\mathrm{GeV}/c$. We note that the result presented here uses a different detector to measure

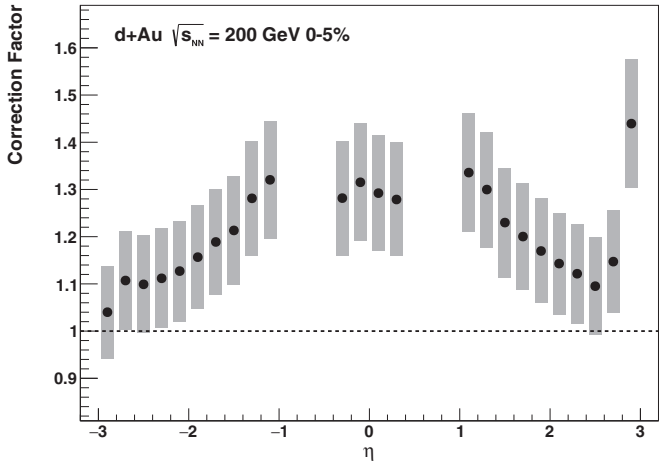


FIG. 6. The correction factor on $v_2(\eta)$ as a function of $\eta$.

the event plane than that used in Ref. [15]. This is a dominant source of systematic uncertainty in the measurement and is therefore largely uncorrelated between the two. Further, at high $p_T$, nonflow effects play a larger role (as discussed later in this paper), and are dependent on the $\Delta\eta$ gap between the region in which the event plane is measured and the region in which the $v_2$ is measured. The increasing nonflow at high $p_T$, which is not estimated in the measurement presented here, potentially explains the modest difference between the two measurements.

### C. Analysis of $v_2$ versus $\eta$ using the event-plane method

The measurement of the $\eta$ dependence of $v_2$ uses the same event-plane method as discussed in Sec. III B. However, to cover the maximum extent in $\eta$, tracks in both the FVTXN and FVTXS are included alongside tracks measured in the central arms. This necessitates using the event plane measured in the BBCS ($\Psi_2^{\rm BBCS}$), rather than the FVTXS. The resolutions of $\Psi_2^{\rm BBCS}$ at each energy are given in Table III.

To calculate the $p_T$-integrated $v_2(\eta)$ we must correct for the detector acceptance and efficiency. This correction is estimated using the (AMPT) model [23], coupled to a full GEANT-3 model [36] of the PHENIX detector. The "true" $v_2$ is calculated in AMPT relative to the parton participant plane, $\Psi_2^{\rm Parton\ Plane}$. The same events are then run through GEANT-3 and the $v_2$ is recalculated using reconstructed tracks, relative to the same $\Psi_2^{\rm Parton\ Plane}$. The resulting correction factor $[\varepsilon^{\rm corr}(\eta)]$ for $d+{\rm Au}$ at $\sqrt{s_{NN}} = 200$ GeV is shown in Fig. 6, and is found to range from 2% to 30%. The correction factors at 62.4 and 39 GeV are similar but show systematic increases at forward rapidity. The uncertainty on the correction factor is estimated by investigating the following effects:

(1) The correction's dependence on the true $v_2$;
(2) The correction's dependence on the true $p_T$ distribution;
(3) The correction's dependence on the simulation-to-data matching.

We investigate the correction's dependence on the true $v_2$ by varying the parton-parton interaction cross section in AMPT from 1.5 to 3.0 mb. This causes a change in the true $v_2$ of ~20%. The correction factor is found to change by a maximum of ±3%. To test the correction factor's sensitivity to the true $p_T$ distribution, the shape of the input $p_T$ distribution is modified such that the mean $p_T$ changes by ±20%. We find that this changes the correction factor by ±8%. Finally, we test the correction's sensitivity to the detailed detector acceptance and efficiency by making tight fiducial cuts, including only regions that agree well between data and simulations. This leads to a maximum change in the correction factor of ±4%. Adding these in quadrature, a ±9.4% systematic uncertainty is assigned on the correction factor. This leads to a systematic uncertainty on the measured $v_2(\eta)$ of $<$ 1–3% that varies with $\eta$.

The resulting, $p_T$-integrated, $v_2(\eta)$ is calculated using

$$v_2(\eta) = \frac{\left\langle \cos 2\left(\phi_{\rm trk}(\eta) - \Psi_2^{\rm BBCS}\right)\right\rangle}{R\left(\Psi_2^{\rm BBCS}\right)\varepsilon^{\rm corr}(\eta)}, \tag{7}$$

where $\phi_{\rm trk}$ is the azimuthal angle of tracks in the FVTX or central arms, $\Psi_2^{\rm BBCS}$ is the second-order azimuthal event plane measured by the BBCS, $R(\Psi_2^{\rm BBCS})$ is the resolution of $\Psi_2^{\rm BBCS}$, and $\varepsilon^{\rm corr}(\eta)$ is the detector acceptance and efficiency correction factor.

The other dominant sources of systematic uncertainty are similar to those detailed for the $v_2(p_T)$ measurement above. (1) Track background in the FVTX is investigated by tightening the $DCA$ track cut. We assign a 2% uncertainty on $v_2(\eta)$ based on this study. (2) The same 1% systematic uncertainty due to event pile-up is assigned based upon the investigation detailed in Sec. III B. (3) Remaining effects due to the 1.0 mrad beam angle are investigated by looking at the difference in the $v_2(\eta)$ as measured by the east and west central arms. We estimate a systematic uncertainty on $v_2(\eta)$ assuming a uniform distribution as $\sigma = \sqrt{\langle v_2^{\rm west}(\eta)\rangle - \langle v_2^{\rm east}(\eta)\rangle}/\sqrt{12}$, which is found to vary with collision energy between 6.5%–33.9%. (4) As in the measurement of $v_2(p_T)$, we cross-check the result, which in this case uses the BBCS event plane, with $v_2(\eta)$ measured using the FVTXS event plane. This allows us to test the agreement at mid and forward rapidities, but not at backward rapidity because tracks cannot be measured in the same region in which the event plane is measured. We find a larger difference between the event-plane results in the forward region and assign a 6.5% uncertainty based on the difference. (5) A systematic uncertainty is assigned based on the uncertainty in the calculated event-plane resolution, as given in Table III. A summary of the systematic uncertainties, and their assigned type, is shown in Table V.

### D. Analysis of $dN_{\rm ch}/d\eta$ versus $\eta$

We begin by measuring the ratio of $dN_{\rm ch}/d\eta$ in central $d+{\rm Au}$ collisions at $\sqrt{s_{NN}} = 62.4$, 39, and 19.6 GeV relative to 0%–5% central $d+{\rm Au}$ collisions at $\sqrt{s_{NN}} = 200$ GeV. The ratio of the raw track distributions are calculated using the analysis cuts described in Sec. II. Variations in the detector performance over time, and as a function of the azimuthal angle, are tested by selecting ten different time periods during the data taking at each energy, as well as four distinct regions

TABLE V. Systematic uncertainties on measurements of $v_2$ versus $\eta$.

| Source | Type | $\sqrt{s_{NN}}$ [GeV] | | |
|---|---|---|---|---|
| | | 200 | 62.4 | 39 |
| Track Background | B | 2.0% | 2.0% | 2.0% |
| Event Pile-up | B | 1.0% | < 1% | < 1% |
| east vs west | B | 4.3% | 13.4% | 33.9% |
| Event-Plane Detector | B | 6.5% | 6.5% | 6.5% |
| Efficiency correction | B | 0–3% | 0–3% | 0–3% |
| Event-Plane Resolution | C | 0.3% | 1.8% | 3.6% |

in $\phi$. The RMS of the ratios for each combination of time period and $\phi$ range are taken as a systematic uncertainty.

When calculating the $dN_{\rm ch}/d\eta$ ratios, it is also important to consider the change in acceptance and efficiency ($A \times \varepsilon$) between collision energies, particularly due to changes in the mean $p_T$ ($\langle p_T \rangle$). We calculate the change in $A \times \varepsilon$ by simulating AMPT events at each collision energy, run through a full GEANT-3 description of the PHENIX detector. The ratio of the resulting $A \times \varepsilon$ distributions for each energy are then calculated as a correction to the ratios in raw data. The sensitivity of the $A \times \varepsilon$ ratio to the true $p_T$ distribution is tested by varying the relative $\langle p_T \rangle$ between energies by $\pm 10\%$. This yields a maximum change in the $A \times \varepsilon$ ratio of 10%, which we assign as a systematic uncertainty. The corrected $dN_{\rm ch}/d\eta$ ratios are shown in Fig. 7.

To calculate the absolutely normalized $dN_{\rm ch}/d\eta$ at each energy, we fix the $dN_{\rm ch}/d\eta$ in 0%–20% $d$ + Au collisions at $\sqrt{s_{NN}} = 200$ GeV to the result previously measured by PHOBOS [37]. The PHOBOS result is in excellent agreement with the previously published $dN_{\rm ch}/d\eta$ at midrapidity measured by PHENIX [38]. This method allows us to reduce the overall systematic uncertainties that arise from calculating an absolutely normalized $A \times \varepsilon$. To calculate the $dN_{\rm ch}/d\eta$ in 0%–5% central $d$ + Au collisions at $\sqrt{s_{NN}} = 200$ GeV, we also need the ratio of $dN_{\rm ch}/d\eta$ in 0%–5% / 0%–20% central $d$ + Au collisions at 200 GeV. This ratio is calculated in the same manner described above. The systematic uncertainties on the PHOBOS measurement are propagated directly to the $dN_{\rm ch}/d\eta$ in 0%–5% central $d$ + Au collisions at 200 GeV.

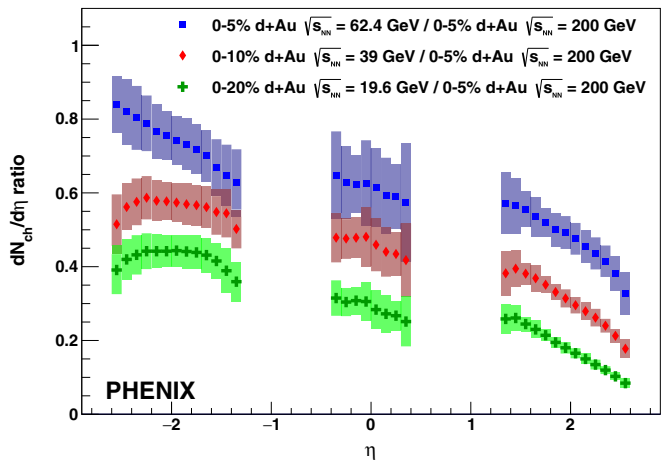


FIG. 7. Ratio of $dN_{\rm ch}/d\eta$ vs. $\eta$ in central $d$ + Au collisions at $\sqrt{s_{NN}} = 62.4$, 39, and 19.6 GeV relative to 0%–5% central $d$ + Au collisions at $\sqrt{s_{NN}} = 200$ GeV. Systematic uncertainties are shown as filled boxes surrounding each point.

## IV. RESULTS AND DISCUSSION

The $v_2(p_T)$ in central $d$ + Au collisions at $\sqrt{s_{NN}} = 200$, 62.4, 39, and 19.6 GeV is shown in Figs. 8(a)–8(d). The $v_2(p_T)$ in centrality bins are shown in Appendix A. A positive $v_2$ signal that increases with increasing $p_T$ is observed in all centrality bins at all four energies.

The $v_2(\eta)$ in central $d$ + Au collisions at $\sqrt{s_{NN}} = 200$, 62.4, and 39 GeV is shown in Figs. 8(e)–8(g). At all three energies we observe a $v_2$ that decreases with increasing $\eta$ between $0 < \eta < 3$. At 200 GeV, the $v_2$ at backward rapidity is similar or greater to that measured at $\eta = 0$. This is reminiscent of the asymmetric $dN_{\rm ch}/d\eta$ measured in $d$ + Au collisions [37]. At 62 GeV the $v_2$ at backward rapidity starts to decrease for $\eta < 0$. This trend is stronger at 39 GeV, where the $v_2$ distribution falls to zero for $\eta = -2.8$. This decrease at backward rapidity may be due to nonflow contributions in regions near where the event plane is measured ($-3.9 < \eta < -3.1$ in this case). This possibility is discussed in more detail in Sec. IV A.

### A. Comparison of $v_2$ results with AMPT calculations

The (AMPT) model [23] combines string melting and then both partonic and hadronic scattering. It has previously been compared to measurements of flow in small collision systems [16,17,24,25] and found to be in good agreement with $p/d/^3$He + Au collisions at $\sqrt{s_{NN}} = 200$ GeV for $p_T < 1\,{\rm GeV}/c$. Following Ref. [39], we use AMPT Version 2.26, which is additionally modified to utilize the Hulthén wave function description of the deuteron and black disk nucleon-nucleon interactions with the Monte Carlo–Glauber component. Further details are discussed in Appendix B. In addition, within AMPT one can run with only partonic scattering (i.e., no hadronic scattering) or with only hadronic scattering (i.e., no partonic scattering), and the results are also shown in Appendix B. In all cases, the charged particle multiplicity in the region $-3.9 < \eta < -3.1$ is used to determine the event centrality class in a manner consistent with the experimental measurements. We begin the discussion by focusing on the most central collisions, as shown in Fig. 8, and return to the full centrality dependence later.

#### 1. Central collisions

Figure 8 shows the $v_2$ calculated relative to the $\Psi_2$ plane calculated from initial partons, labeled $v_2\{\text{Parton Plane}\}$.[1] By calculating $v_2$ relative to the parton plane, we can isolate the

[1] We note that Ref. [39] includes AMPT calculations of $v_2(p_T)$ relative to the initial *nucleon* positions for $b < 2$ fm $d$ + Au collisions at the energies measured here. The results are broadly similar to those shown here.

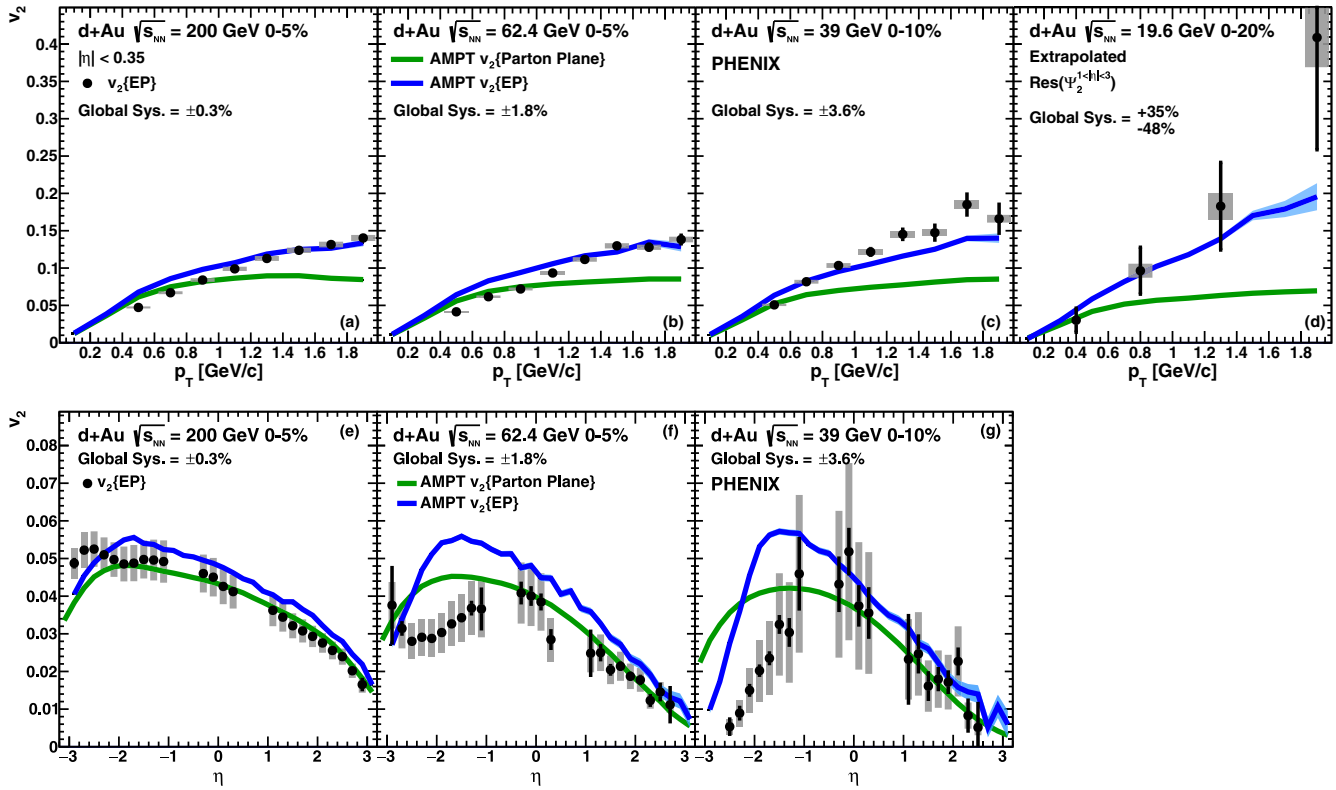


FIG. 8. The value of $v_2$ as a function of $p_T$ in central $d$ + Au collisions at $\sqrt{s_{NN}} = 200$ (a), 62.4 (b), 39 (c), and 19.6 (d) GeV. $v_2$ as a function of $\eta$ in central $d$ + Au collisions at $\sqrt{s_{NN}} = 200$ (e), 62.4 (f), and 39 (g) GeV. The lower [green] curves show calculations from the AMPT model [23] where the $v_2$ is calculated relative to the parton plane. The upper [blue] curves show calculations from the AMPT model, where the $v_2$ is calculated using the event-plane method, as described in the text.

$v_2$ that is truly coupled to the initial geometry, or what we refer to as flow. At 200 and 62.4 GeV, AMPT provides a reasonable description of the data for $p_T < 1\,\mathrm{GeV}/c$ and under-predicts the data for $p_T > 1\,\mathrm{GeV}/c$. At 39 and 19.6 GeV AMPT under-predicts the data at all but the lowest $p_T$. We further find good agreement between $v_2(\eta)$ and $v_2\{\text{Parton Plane}\}$ at mid and forward rapidities at all three collision energies. At backward rapidity we find good agreement at 200 GeV, but AMPT does not show the same fall-off as seen in the data at 62.4 and 39 GeV.

Because AMPT is a full event generator, we can not only determine $v_2\{\text{Parton Plane}\}$, but also mimic in detail the experimental measurement using only the final-state particles. We use the same event-plane method as used in the data analysis, matching the nominal pseudorapidity ranges of the detectors rather than a full GEANT-3 simulation of the detector response. This result, labeled as $v_2\{\text{EP}\}$, includes not only flow, but also nonflow correlations as modeled within AMPT. The results are shown in Fig. 8. As a function of $p_T$, the $v_2\{\text{EP}\}$ calculations are similar to $v_2\{\text{Parton Plane}\}$ for $p_T < 0.5\,\mathrm{GeV}/c$. For $p_T > 0.5\,\mathrm{GeV}/c$ the event-plane results produce a larger $v_2$ signal, which is in better agreement with the data. This difference highlights the contributions from nonflow that, in AMPT, increase with increasing $p_T$ and decreasing collision energy.

When looking at $v_2(\eta)$, shown in Fig. 8, we find that the AMPT event-plane results are in good agreement with the measured data for $\eta > 0$ at all three collision energies. At 200 GeV we see a roughly constant increase versus $\eta$ of the $v_2\{\text{EP}\}$ compared to the $v_2\{\text{Parton Plane}\}$, indicating a roughly 15% increase in the $v_2$ with the addition of nonflow. Both calculations are in agreement with the data within uncertainties. At 62.4 and 39 GeV we see a larger increase in the event-plane result versus the parton plane result compared to the 200 GeV. What is particularly interesting is that AMPT shows a decrease in the event-plane result for $\eta < -2$ that is stronger for 39 GeV than 62.4 GeV, and drops below the parton plane result at $\eta \approx -2.5$. While this decrease doesn't occur at the same $\eta$, and is only in qualitative agreement with the data, it points out that within AMPT this feature only arises when you combine flow and nonflow. When using the event-plane method at these low energies, AMPT predicts a larger deviation between the true flow signal and the experimentally observed flow signal as the $\Delta\eta$ between the region in which the tracks are measured and the region in which the event plane is measured decreases. We further caution that, while AMPT qualitatively agrees with our measurements over a broad range in collision energy and particle kinematics, we cannot use it to definitively separate flow from nonflow, but rather to give some insight and possible intuition for interpreting the experimental results in regions where we are currently unable to perform the separation experimentally.

Using AMPT, we can also study whether our measured $v_2(\eta)$ is likely to arise solely from nonflow contributions. By setting the partonic and hadronic interaction cross sections to

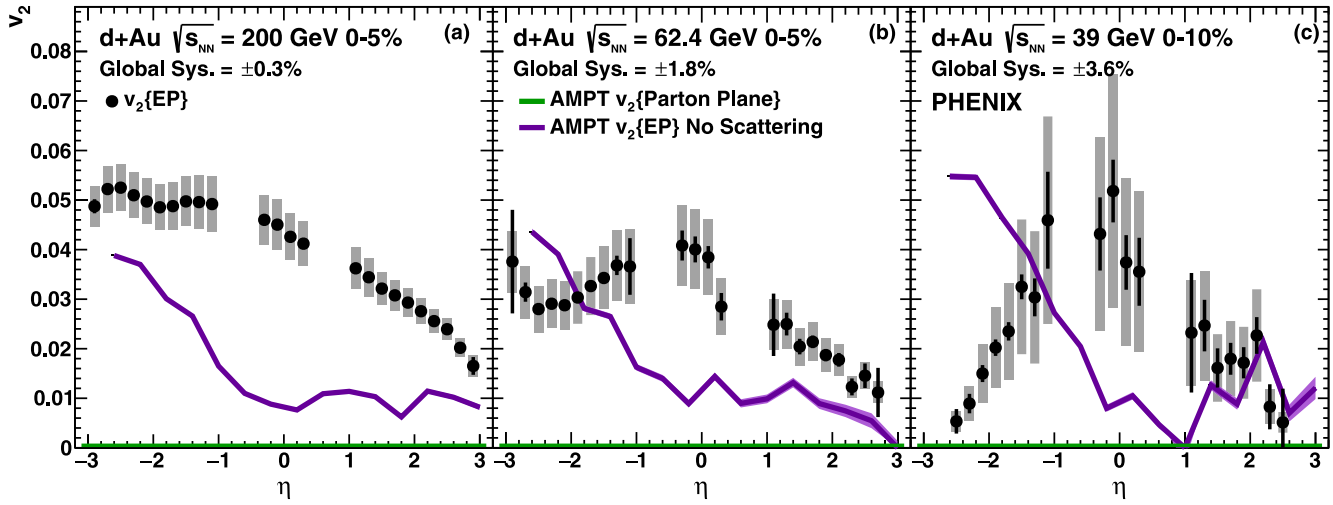


FIG. 9. The value of $v_2$ as a function of $\eta$ in central $d$ + Au collisions at $\sqrt{s_{NN}} = 200$, 62.4, and 39 GeV compared to calculations from the AMPT model [23] in which both the partonic and hadronic scatterings have been turned off. The upper [purple] curves show calculations from the AMPT model using the event-plane method as described in the text. The lower [green] curves ($v_2 = 0$ in all cases) show calculations from AMPT where $v_2$ is calculated relative to the parton plane.

zero within AMPT, we eliminate all interactions that translate initial-state geometry to final-state momentum correlations. This is shown explicitly in Fig. 9, where $v_2\{\text{Parton Plane}\} = 0$ at all $\eta$. However, even with all partonic and hadronic scattering turned off, nonflow correlations can still give rise to a $v_2\{\text{EP}\}$ signal. This is shown by the upper [purple] curves in Fig. 9. Note that in this mode the event plane angle arises only from nonflow correlations and has no connection to the initial geometry (i.e., the parton plane). In this case the resolution of the event plane is roughly a factor of 3 lower than with partonic and hadronic interactions. At all three energies, $v_2\{\text{EP}\} < 0.01$ for $\eta > 0$ within AMPT with partonic and hadronic scattering switched off. This region is far removed ($\Delta\eta > 3.1$) from the region in which the event plane is constructed and is therefore unlikely to contain correlations from jets or particle decays. In the region $\eta < 0$, however, an increasing $v_2\{\text{EP}\}$ is observed. This indicates, as expected, that the smaller the $\Delta\eta$ gap the larger the effects of nonflow. In all cases, the measured $v_2(\eta)$ for $\eta > 0$ is larger than the $v_2\{\text{EP}\}$ from AMPT with nonflow correlations only. This extends to $\eta < 0$ in central collisions at 200 GeV. The small values of the $v_2\{\text{EP}\}$ from nonflow correlations only lends further confidence that the low $p_T$ and $\eta > 0$ region is dominated by flow correlations linked to the initial geometry of the collision. We note that it is not clear how this large increasing $v_2\{\text{EP}\}$ signal at $\eta < 0$ with partonic and hadronic scattering turned off (nonflow only) turns into a decreasing $v_2\{\text{EP}\}$ signal at $\eta < 0$ when partonic and hadronic scattering are turned on (flow + nonflow). Presumably this is due to detailed interactions between the angle of the parton plane and the dominant axis of the nonflow on an event-by-event level within AMPT.

#### 2. *Centrality dependence*

We now return to the centrality dependence of $v_2(p_T)$. From the comparison of $v_2(p_T)$ in central collisions we can separate the $p_T$ spectra into two regions: (1) $p_T < 1\,\text{GeV}/c$ where AMPT parton and event plane results are roughly similar. (2) $p_T > 1\,\text{GeV}/c$ where the event plane results, which include nonflow contributions, yield a larger $v_2$ than that calculated with the parton plane. We choose two particular $p_T$ bins, $0.6 < p_T < 0.8$ and $2.0 < p_T < 2.5$, and investigate the centrality dependence of the $v_2$ at $\sqrt{s_{NN}} = 200$, 62.4, and 39 GeV in comparison with the results from AMPT, as shown in Fig. 10. Note that while the event plane resolution uncertainty is a global scale uncertainty when plotting $v_2$ as a function of $p_T$, when plotting $v_2$ as a function of centrality it becomes a type B systematic uncertainty and is added in quadrature with the other type B systematic uncertainties in Fig. 10.

Starting with the low $p_T$ $v_2$, AMPT shows similar results between the parton and event planes, indicating within AMPT that the flow dominates in this $p_T$ region. The AMPT results also predict a decrease in the $v_2$ results toward more peripheral collisions, as expected from the decrease in the mean ellipticity of the initial geometry and lower particle multiplicity. This is contrary to the trends in the data where the values of $v_2$ increase in the most peripheral collisions. This increase is more pronounced in the lower-energy data and it may indicate that nonflow contributions are larger in the data than in AMPT. The $v_2$ values measured in the centrality range up to 20% are in good agreement with the predictions from AMPT.

At high $p_T$, AMPT predicts a significantly larger $v_2$ calculated relative to the event plane compared to the parton plane, indicating significant contributions from nonflow correlations. At 39 and 62.4 GeV, we observe a $v_2$ that increases with more peripheral collisions. At 62.4 GeV, AMPT well reproduces this increasing behavior. At 200 GeV, however, AMPT over-predicts the observed increase, while under-predicting the increase at 39 GeV.

### B. Comparison of $v_2$ results with hydrodynamic calculations

Shown in Fig. 11 are predictions from the SONIC and superSONIC models for $v_2(p_T)$ at midrapidity [39]. The SONIC

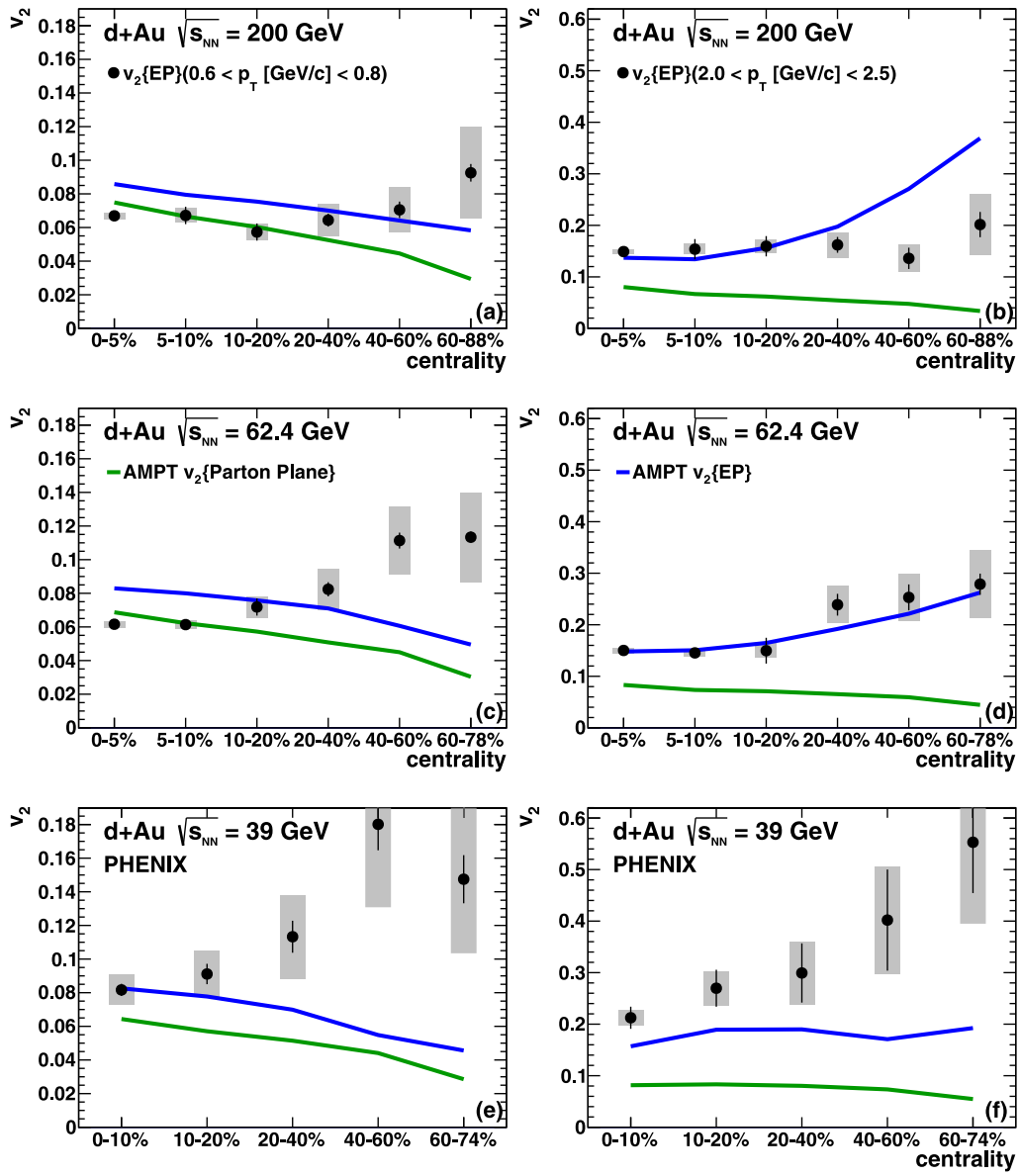


FIG. 10. The value of $v_2$ as a function of centrality (a), (c), (e) at $0.6 < p_T[\mathrm{GeV}/c] < 0.8$ and (b), (d), (f) at $2.0 < p_T\ [\mathrm{GeV}/c] < 2.5$ in $d+\mathrm{Au}$ collisions at $\sqrt{s_{NN}} =$ (a), (b) 200, (c), (d) 62.4, and (e), (f) 39 GeV. The upper [blue] curves show calculations from the AMPT model [23], where the $v_2$ is calculated using the event plane method as described in the text. The lower [green] curves show AMPT calculations where the $v_2$ is calculated relative to the parton plane.

model [41] uses Monte Carlo–Glauber initial conditions to determine the energy density distribution. For these calculations, $b < 2$ fm was used to represent the central-event category. While $b < 2$ fm is not a direct match for our central multiplicity bins, the resulting $\varepsilon_2$ values are consistent with those given in Table II. The initial energy density is tuned such that the $dN_{\mathrm{ch}}/d\eta$ at midrapidity matches the values given in Table VI. The Glauber initial conditions are followed by viscous hydrodynamics with $\eta/s = 1/4\pi$, and at $T =$ 170 MeV the transition to a hadron cascade. The superSONIC model [42] additionally includes pre-equilibrium dynamics. At 200 and 62.4 GeV, both calculations are in excellent agreement with the data, with superSONIC providing a slightly better description for $p_T > 1\,\mathrm{GeV}/c$. At 39 and 19.6 GeV, both calculations under-predict the data for $p_T > 0.5\,\mathrm{GeV}/c$. This difference may be due to the increasing contributions of nonflow present in the data at high $p_T$ and lower collision energies, which is not accounted for in these calculations. Without a reliable estimate of the nonflow contribution, the data is unable to distinguish between SONIC and superSONIC.

Figure 11(e) includes hydrodynamic predictions of the $\eta$ dependence of $v_2$ in $d+\mathrm{Au}$ collisions at $\sqrt{s_{NN}} = 200$ GeV from Bozek and Broniowski [40]. These calculations utilize MC Glauber initial conditions, evolved with event-by-event $3+1$D viscous hydrodynamics, followed by statistical hadronization at freeze-out. The calculations are in good agreement with the data for $\eta > -2$ but start to under predict the data in the region $-3 < \eta < -2$.

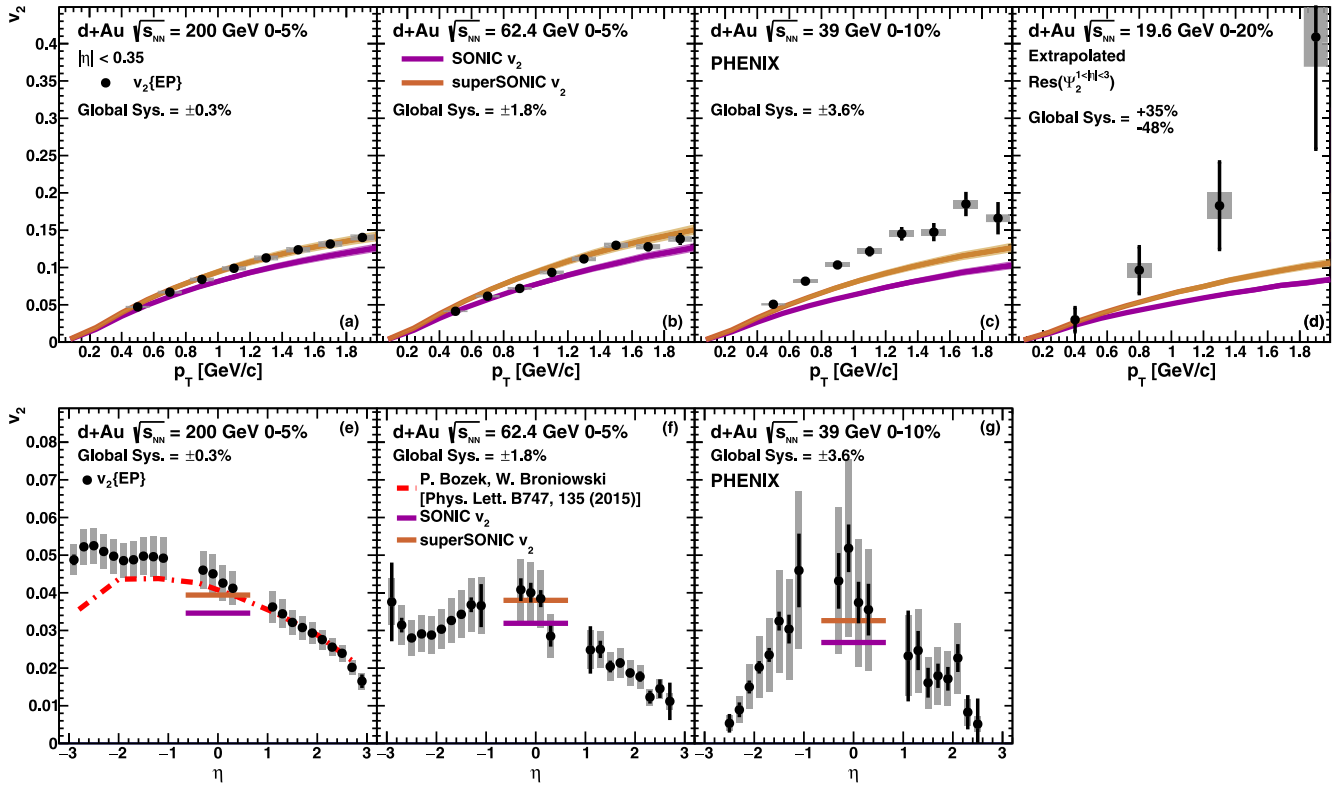


FIG. 11. The value of $v_2$ as a function of $p_T$ in central $d+$Au collisions at $\sqrt{s_{NN}}$ = (a) 200, (b) 62.4, (c) 39, and (d) 19.6 GeV. $v_2$ as a function of $\eta$ in central $d+$Au collisions at $\sqrt{s_{NN}}$ = (e) 200, (f) 62.4, and (g) 39 GeV. At midrapidity, the [lower] purple and upper [orange] curves show theoretical calculations from SONIC and superSONIC [39], respectively. The dashed [red] curve in panel (e) shows hydrodynamic predictions from Ref. [40].

### C. Comparison of $dN_{ch}/d\eta$ results with AMPT calculations

The measurements of $dN_{ch}/d\eta$ versus $\eta$ in central $d+$Au collisions at $\sqrt{s_{NN}}$ = 200, 62.4, 39, and 19.6 GeV are shown in Fig. 12. At all four energies, the $dN_{ch}/d\eta$ at backward rapidity is larger than that at forward rapidity, and the overall $dN_{ch}/d\eta$ decreases at all $\eta$ with decreasing energy. Also shown in Fig. 12 are calculations from AMPT in the same centrality classes, as well as a prediction from Bozek and Broniowski [40] for 0%–5% central $d+$Au collisions at $\sqrt{s_{NN}}$ = 200 GeV. At 200 GeV, AMPT agrees with the data well at mid and forward rapidities, while over-predicting the data at backward rapidity. The calculation from Bozek and Broniowski agrees with the data at mid to forward rapidity, while under-predicting the data at backward rapidities. It is worth noting that calculations from Bozek and Broniowski are substantially lower than the AMPT calculations for $\eta < -1$. This is potentially due to the centrality determination in AMPT (and data), which selects on multiplicity in the region $-3.9 < \eta < -3.1$, which may naturally cause an autocorrelation with the $dN_{ch}/d\eta$ in the region $-3 < \eta < -1$. At the lower three energies, AMPT matches the data well at forward psuedorapidity only and over-predicts the data at midrapidity.

TABLE VI. The charged particle multiplicity ($dN_{ch}/d\eta$) at midrapidity for central $d+$Au collisions at $\sqrt{s_{NN}}$ = 200, 62.4, 39, and 19.6 GeV.

| $\sqrt{s_{NN}}$ [GeV] | Centrality | Data | AMPT | (super)SONIC |
|---|---|---|---|---|
| 200 | 0%–5% | $20.3 \pm 1.5$ | 19.3 | $20.2 \pm 2$ |
| 62.4 | 0%–5% | $12.4 \pm 2.4$ | 16.1 | $15.0 \pm 2$ |
| 39 | 0%–10% | $9.3 \pm 1.6$ | 14.0 | $11.6 \pm 2$ |
| 19.6 | 0%–20% | $5.8 \pm 1.1$ | 9.7 | $9.7 \pm 2$ |

We next turn to investigating whether there is a scaling of $v_2 \propto dN_{ch}/d\eta$. Figures 13(a)–13(c) show the measured $v_2(\eta)$ overlaid with the $dN_{ch}/d\eta$, where the $dN_{ch}/d\eta$ is arbitrarily scaled at each energy to match the $v_2$ at forward rapidity. We have chosen to match the $dN_{ch}/d\eta$ to the $v_2$ at $\eta > 0$, as we expect the $v_2$ in this region to have the lowest contribution from nonflow, as discussed in Sec. IV A. The required scaling factor increases with decreasing energy, with scaling factors of 0.0020, 0.0025, and 0.0030 at 200, 62.4, and 39 GeV, respectively.

Figures 13(d)–13(f) show the $v_2${Parton Plane} from AMPT overlaid with the scaled $dN_{ch}/d\eta$, also from AMPT, using the same scaling factors determined from data. Additionally, Fig. 13(d) shows the overlay of the calculations of $v_2$ and $dN_{ch}/d\eta$ from Bozek and Broniowski, where $dN_{ch}/d\eta$ is scaled by the same factor of 0.0020.

Starting with the 200 GeV results in Figs. 13(a) and 13(d), we find that when using a constant scaling factor across $\eta$, the scaled $dN_{ch}/d\eta$ and $v_2(\eta)$ agree well within uncertainties. The increase in the $v_2$ from forward to backward rapidity is matched by the increase in the $dN_{ch}/d\eta$. In comparison, the

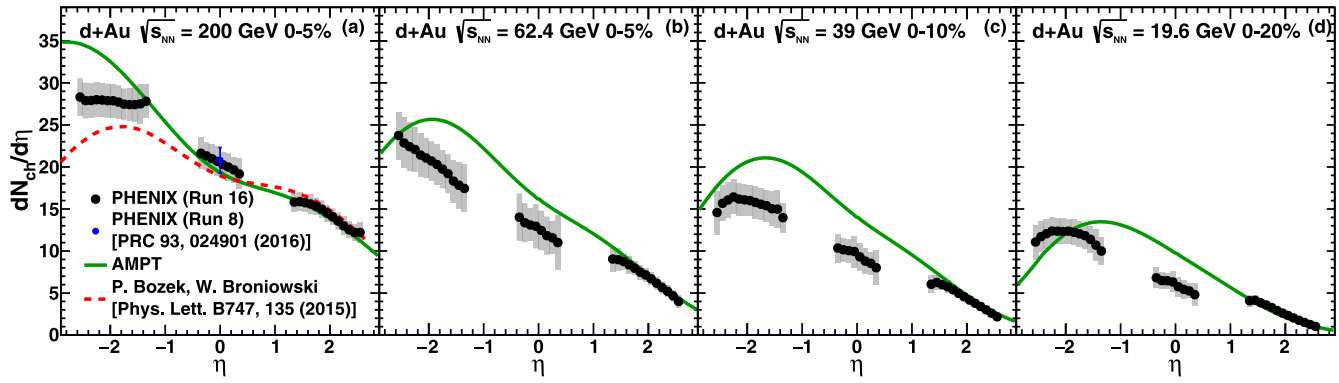


FIG. 12. The $dN_{\rm ch}/d\eta$ vs. $\eta$ in central $d+$Au collisions at $\sqrt{s_{NN}}$ = (a) 200, (b) 62.4, (c) 39, and (d) 19.6 GeV. The solid [green] curves are the AMPT calculations in similar centrality bins. The dashed [red] curve in panel (a) is a hydrodynamic prediction from Ref. [40] for 0%–5% central $d+$Au collisions at $\sqrt{s_{NN}} = 200$ GeV.

AMPT shows an approximate scaling only at forward rapidity, although a better match is found when using a scaling factor of 0.0022, rather than 0.0020. The scaled $dN_{\rm ch}/d\eta$ breaks from the $v_2${Parton Plane} for $\eta < 1$, indicating that within AMPT there is no direct scaling of the $dN_{\rm ch}/d\eta$ and $v_2${Parton Plane}. Similarly, the calculations by Bozek and Broniowski show an approximate scaling at forward rapidity, and a modest scale breaking at backward rapidities.

At 62.4 and 39 GeV, we find that the scaled $dN_{\rm ch}/d\eta$ and $v_2(\eta)$ agree within uncertainties at mid and forward rapidities. At backward rapidity, however, the scaled $dN_{\rm ch}/d\eta$ is significantly larger than the $v_2$ for the same scaling factor. It is notable that AMPT $v_2$ does not scale with $dN_{\rm ch}/d\eta$ at backward rapidity at any energy. As discussed in Sec. IV A, AMPT calculations indicate that there could be an anticorrelation effect at backward rapidity that decreases the observed $v_2$ relative to the true $v_2$ when using the event-plane method.

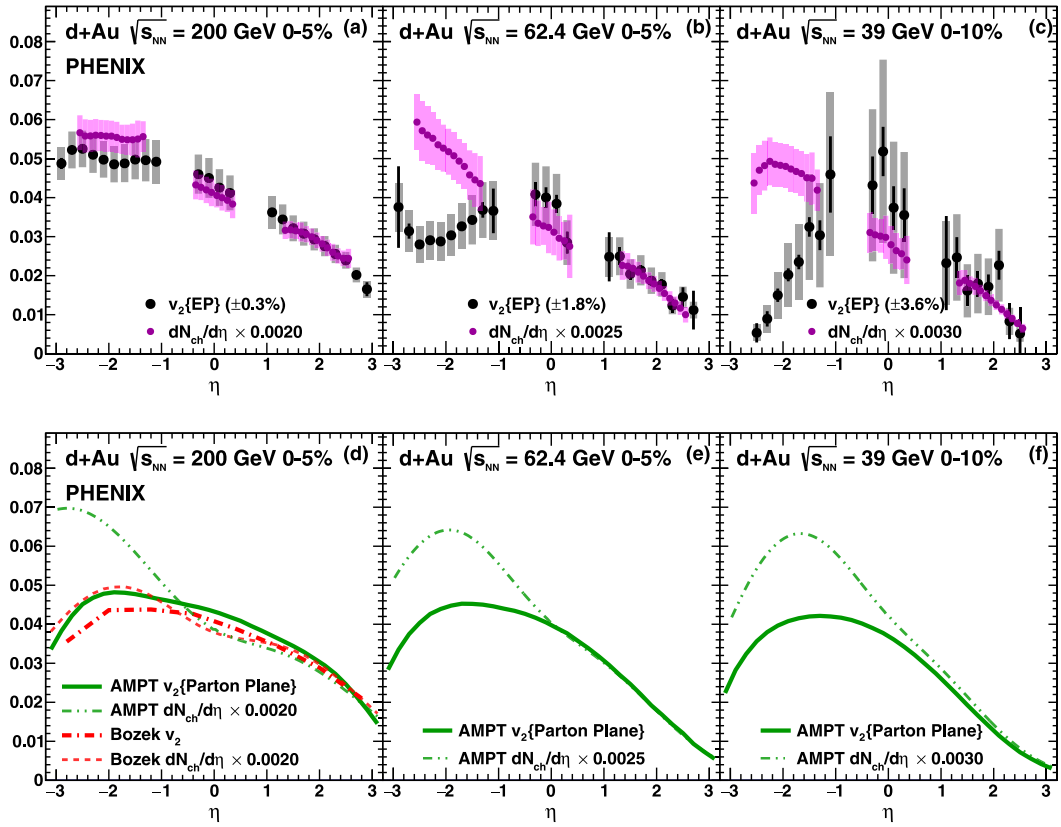


FIG. 13. The $v_2$ vs. $\eta$ and $dN_{\rm ch}/d\eta$ vs. $\eta$, scaled to match the $v_2$ in $1.0 < \eta < 3.0$, for central $d+$Au collisions at $\sqrt{s_{NN}}$ = (a) 200, (b) 62.4, and (c) 39 GeV. The dashed-double-dot and solid [green] curves in panels (d)–(f) show the results from AMPT using the same scaling factors determined from the data. The dash and dash-dot [red] curves in panel (d) show the hydrodynamic predictions from Ref. [40] in 0%–5% central $d+$Au collisions at $\sqrt{s_{NN}} = 200$ GeV, again using the same scaling factor determined from the data.

Further investigations into potential nonflow anticorrelations in the event-plane method with a small $\Delta\eta$ gap would be useful to shed more light on these possible conclusions.

## V. SUMMARY AND CONCLUSIONS

PHENIX has presented new measurements of the second-order flow coefficient $v_2$ in bins of centrality in $d+\mathrm{Au}$ collisions at $\sqrt{s_{NN}} = 200$, 62.4, 39, and 19.6 GeV as a function of $p_T$ and $\eta$. We find that at mid to forward rapidities and low $p_T$, $v_2$ appears to be dominated by flow, where we define flow as the translation of initial geometry to final-state momentum anisotropy via interactions between medium constituents. In contrast, at backward rapidity and high $p_T$, nonflow becomes an increasingly significant contribution.

It would be interesting to compare the $v_2$ results measured in the $d+\mathrm{Au}$ beam energy scan with those measured in $p+p$ and $p+\mathrm{Pb}$ collisions at the LHC. The multiplicity ranges probed in the $d+\mathrm{Au}$ beam energy scan are comparable to those in $p+p$ collisions at the LHC, which range from $dN_{\mathrm{ch}}/d\eta \approx 4$ in MB collisions to $dN_{\mathrm{ch}}/d\eta > 80$ in very high-multiplicity events [43]. Comparing the different systems at similar multiplicities, but vastly different collision energies and initial geometries, may give further insight into the underlying mechanism generating the $v_2$ signal. We further present measurements of $dN_{\mathrm{ch}}/d\eta$ versus $\eta$ at all four energies. At 200 GeV, we find that a constant scale factor yields agreement between the measured $v_2$ versus $\eta$ and the shape of $dN_{\mathrm{ch}}/d\eta$. At 62.4 and 39 GeV, the shapes of $v_2$ and $dN_{\mathrm{ch}}/d\eta$ match well at mid and forward rapidity; however, the $dN_{\mathrm{ch}}/d\eta$ increases at backward rapidity while the $v_2$ decreases. This presents a different picture than that observed at 200 GeV and may be due to anticorrelations present in the event-plane method when the $\Delta\eta$ gap becomes small.

These results provide further evidence that the $v_2$ measured in small systems arises from initial geometry coupled to interactions between medium constituents, whether described by parton scattering or hydrodynamics. In $d+\mathrm{Au}$ collisions at $\sqrt{s_{NN}} = 200$ GeV, these flow effects dominate and they continue to play a significant, though less dominant role all the way down to $\sqrt{s_{NN}} = 19.6$ GeV.

## ACKNOWLEDGMENTS

We thank the staff of the Collider-Accelerator and Physics Departments at Brookhaven National Laboratory and the staff of the other PHENIX participating institutions for their vital contributions. We acknowledge support from the Office of Nuclear Physics in the Office of Science of the Department of Energy, the National Science Foundation, Abilene Christian University Research Council, Research Foundation of SUNY, and Dean of the College of Arts and Sciences, Vanderbilt University (USA), Ministry of Education, Culture, Sports, Science, and Technology and the Japan Society for the Promotion of Science (Japan), Conselho Nacional de Desenvolvimento Científico e Tecnológico and Fundação de Amparo à Pesquisa do Estado de São Paulo (Brazil), Natural Science Foundation of China (People's Republic of China), Croatian Science Foundation and Ministry of Science and Education (Croatia), Ministry of Education, Youth and Sports (Czech Republic), Centre National de la Recherche Scientifique, Commissariat à l'Énergie Atomique, and Institut National de Physique Nucléaire et de Physique des Particules (France), Bundesministerium für Bildung und Forschung, Deutscher

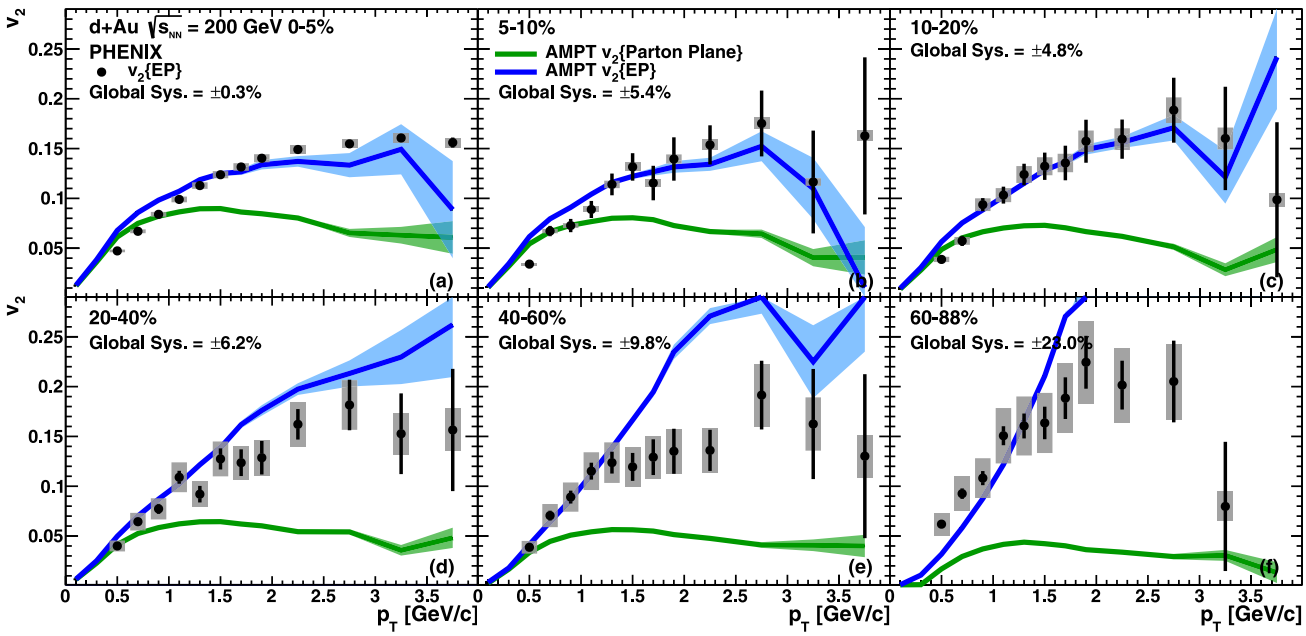


FIG. 14. For $d+\mathrm{Au}$ collisions at $\sqrt{s_{NN}} = 200$ GeV, the value of $v_2$ as a function of $p_T$ in (a) 0%–5%, (b) 5%–10%, (c) 10%–20%, (d) 20%–40%, (e) 40%–60%, and (f) 60%–88%. The upper [blue] curves show calculations from the AMPT model [23], where the $v_2$ is calculated using the event-plane method, as described in the text. The lower [green] curves show AMPT calculations, where the $v_2$ is calculated relative to the parton plane.

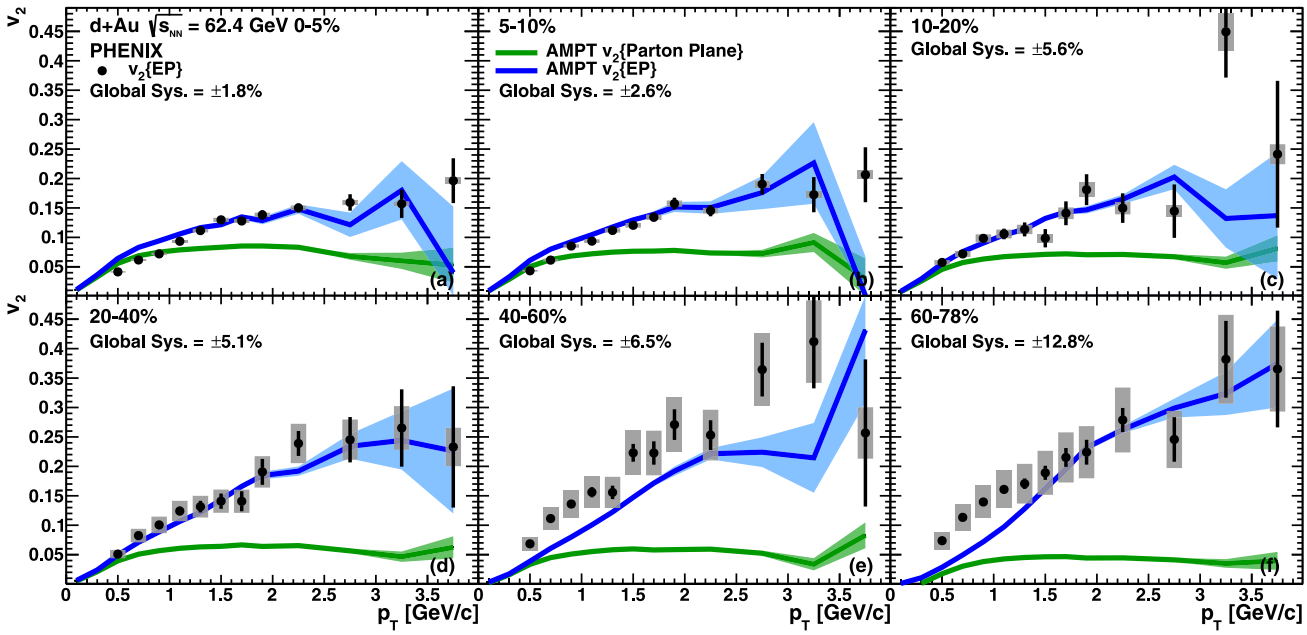


FIG. 15. For $d$ + Au collisions at $\sqrt{s_{NN}} = 62.4$ GeV, descriptions of the symbols and curves are the same as in Fig. 14.

Akademischer Austausch Dienst, and Alexander von Humboldt Stiftung (Germany), J. Bolyai Research Scholarship, EFOP, the New National Excellence Program (ÚNKP), NKFIH, and OTKA (Hungary), Department of Atomic Energy and Department of Science and Technology (India), Israel Science Foundation (Israel), Basic Science Research Program through NRF of the Ministry of Education (Korea), Physics Department, Lahore University of Management Sciences (Pakistan), Ministry of Education and Science, Russian Academy of Sciences, Federal Agency of Atomic Energy (Russia), VR and Wallenberg Foundation (Sweden), the US Civilian Research and Development Foundation for the Independent States of the Former Soviet Union, the Hungarian American Enterprise Scholarship Fund, the US-Hungarian Fulbright Foundation, and the US-Israel Binational Science Foundation.

## APPENDIX A: CENTRALITY DEPENDENCE OF $v_2(p_T)$

The $v_2(p_T)$ in centrality bins for $d$ + Au collisions at $\sqrt{s_{NN}} = 200$, 62.4, and 39 GeV are shown in Figs. 14–16, respectively.

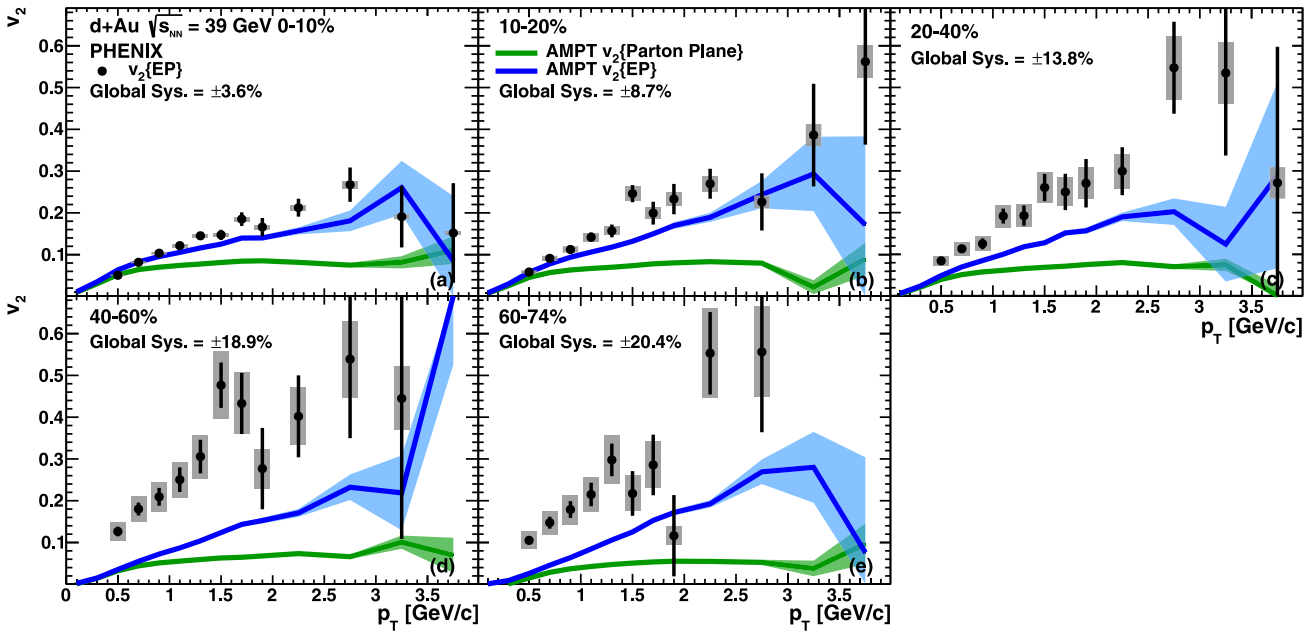


FIG. 16. For $d$ + Au collisions at $\sqrt{s_{NN}} = 39$ GeV, descriptions of the symbols and curves are the same as in Fig. 14.

TABLE VII. Nondefault parameter values used when running AMPT.

| Parameter | Value |
|---|---|
| ISOFT | 4 |
| PARJ(41) | 2.2 |
| PARJ(42) | 0.5 |
| Parton screening mass | 6.4528$d$0 (0.75 mb) |
| $\alpha$ in parton cascade | 0.47140452$d$0 |
| ihjsed | 11 |

## APPENDIX B: AMPT DETAILS

The AMPT calculations shown in this work are generated following Ref. [39]. We use AMPT Version 2.26, which is additionally modified to utilize the Hulthén wave function description of the deuteron and black disk nucleon-nucleon interactions with the Monte Carlo–Glauber component. The input AMPT parameters which are tuned outside the default values are shown in Table VII. Unlike Ref. [39], which uses a parton interaction cross section of 1.50 mb, we use a parton interaction cross section of $\sigma_{\text{parton}} = 0.75$ mb, as we find it provides a better description of the centrality binned data.

In addition to the full AMPT calculations with both partonic and hadronic scattering shown in Figs. 8 and 14–16, we provide calculations for the following three cases:

(1) N.S.—Both partonic scattering and hadronic scattering turned off (i.e., no scattering);
(2) P.S.—Partonic scattering only;
(3) H.S.—Hadronic scattering only.

To turn off hadronic scattering we turn off the hadron cascade (NTMAX = 3). To turn off partonic scattering we set the parton interaction cross section to 0 mb. Figures 17 and 18 show the results for central $d$ + Au collisions.

Figure 17 shows the results from AMPT for $v_2$ as a function of $p_T$ and pseudorapidity using the parton plane method, which yields a pure flow result with respect to initial geometry. Focusing on the $p_T$ dependence in Fig. 17 (upper panels), the hadronic scattering only scenario results in larger $v_2$ compared to the partonic scattering only scenario at low $p_T < 1\,\text{GeV}/c$ and then a comparable $v_2$ for higher $p_T$. Note that these contributions cannot simply be summed to achieve the result with both partonic and hadronic scattering because

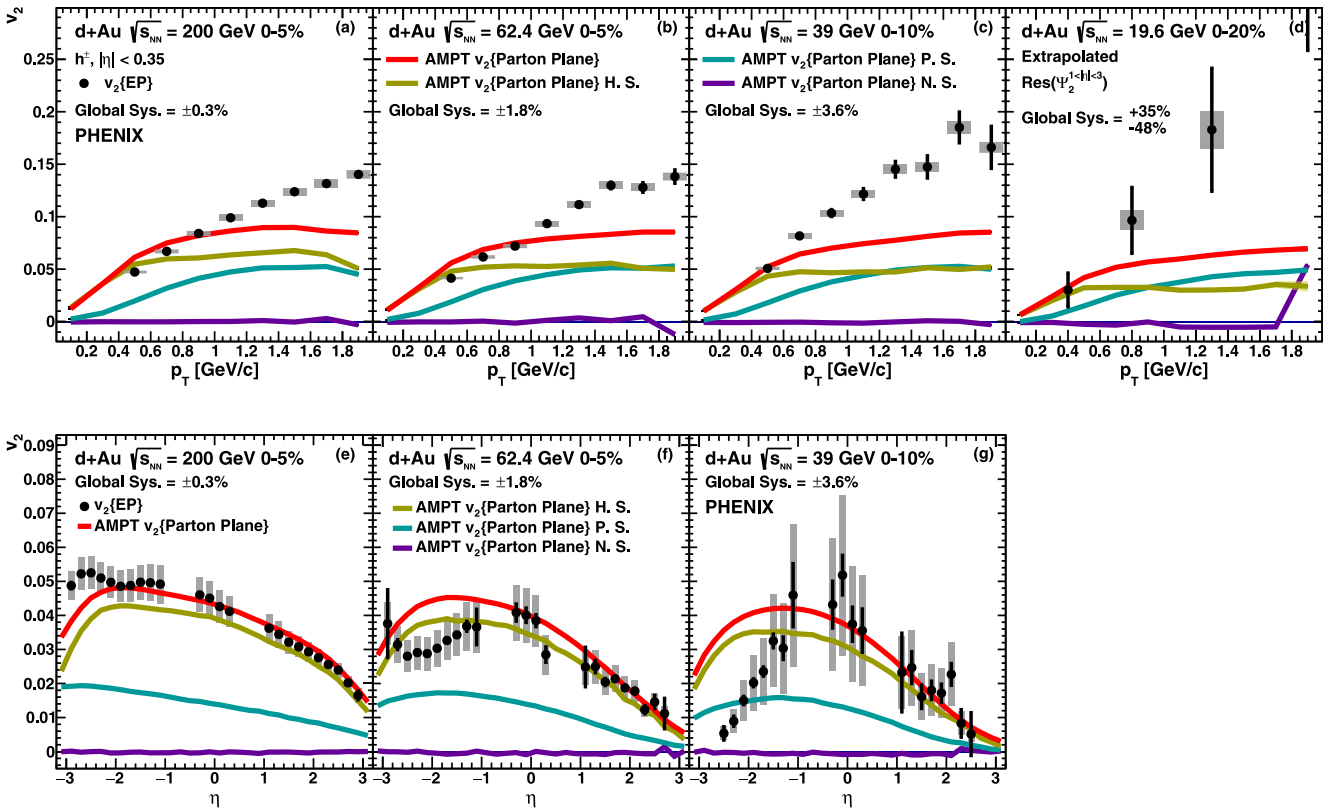


FIG. 17. (a)–(d) the value of $v_2$ vs. $p_T$ in central $d$ + Au collisions at $\sqrt{s_{NN}} = 200$, 62.4, 39, and 19.6 GeV. (e)–(g) the value of $v_2$ vs. $\eta$ in central $d$ + Au collisions at $\sqrt{s_{NN}} = 200$, 62.4, and 39 GeV. The curves are calculations from AMPT under different conditions. With ordering of curves from top to bottom (a)–(d) at $p_T = 0.6$ and (e)–(g) at $\eta = 0$, the uppermost [red] curve is AMPT with both partonic and hadronic scattering; the upper-middle [yellow] curve is AMPT with hadronic scattering only (H.S.); the lower-middle [cyan] curve is AMPT with partonic scattering only (P.S.); and the lowest [purple] curve is AMPT with no scattering (N.S.). For all AMPT curves, the $v_2$ is calculated relative to the initial parton plane.

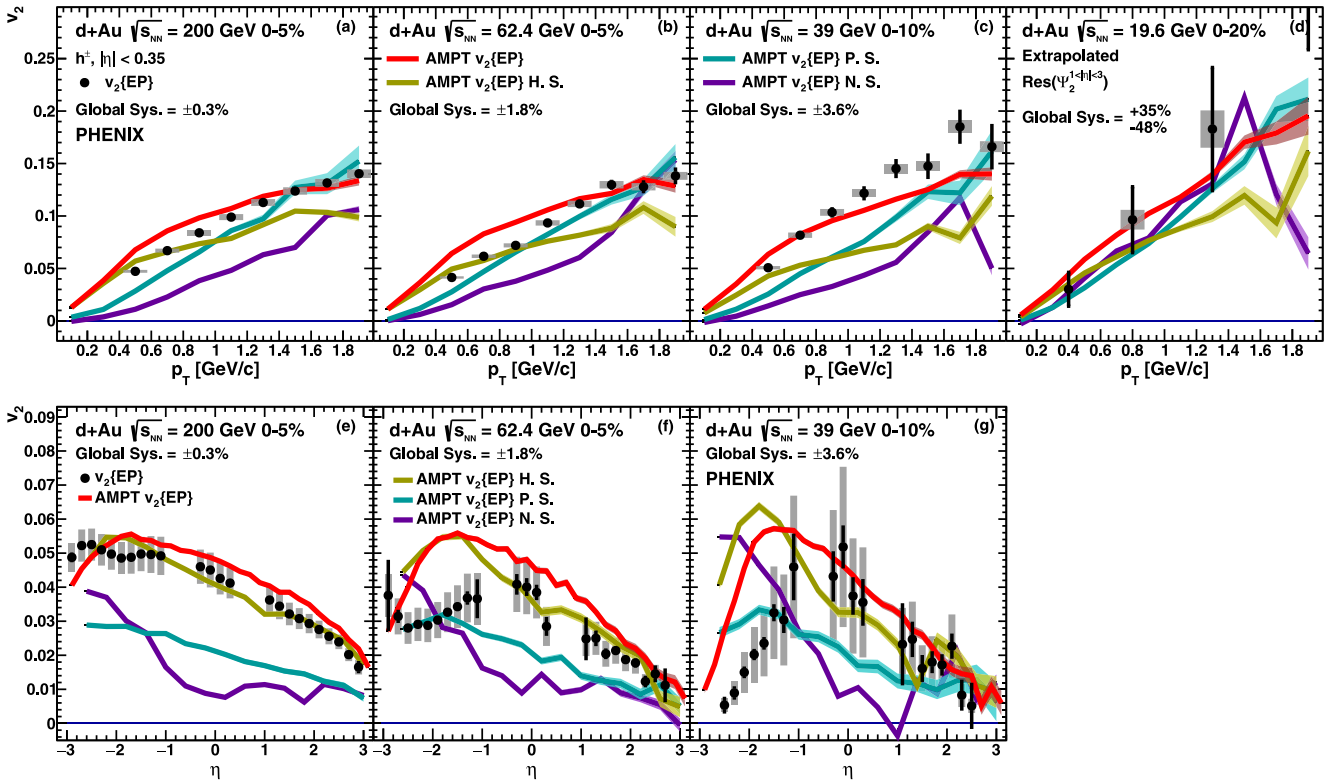


FIG. 18. The description of all symbols and curves are the same as in Fig. 17, except that for all AMPT curves the $v_2$ is calculated relative to the final-state event plane.

the space-time input for the hadronic scattering stage changes depending on whether there is or is no partonic scattering stage. The significantly larger $v_2$ in the hadronic-scattering-only scenario at low $p_T$ is most clearly seen in Fig. 17 (lower panels) because the $v_2$ as a function of pseudorapidity is integrated over all $p_T$.

At high $p_T$, the partonic-scattering-only scenario has a more comparable contribution to the hadronic-scattering-only scenario, with it being slightly smaller at 200 GeV and slightly larger at 39 GeV. Because the AMPT model employs a formation time for partons such that higher $p_T$ partons start scattering earlier in time, it makes sense that this contributes more significantly. It is notable that in Ref. [39], it was shown that the parton scattering began to dominate for $p_T > 0.8\,\mathrm{GeV}/c$. This difference is likely due to the larger parton interaction cross section of 1.50 mb used in Ref. [39]. As the collision energy decreases, the partonic scattering contributes more to the overall $v_2$ signal. As discussed in Sec. IV A, the no scattering case has $v_2\{\text{Parton Plane}\} = 0$ by definition, as it no longer has the ability to translate initial geometry to momentum anisotropy.

Figure 18 shows results calculated using the event-plane method ($v_2\{\text{EP}\}$), i.e., simulating the experimental method of extracting $v_2$. The general statement above that hadronic scattering dominates at low $p_T$ while partonic scattering contributes mainly at higher $p_T$ remains true down to $\sqrt{s_{NN}} = 39$ GeV. However, as discussed in Sec. IV A, the case with both partonic and hadronic scattering turned off now shows a nonzero $v_2\{\text{EP}\}$ signal. This $v_2\{\text{EP}\}$ result without scattering indicates that nonflow is small at low $p_T$ but grows with increasing $p_T$. For collision energies of 39 GeV and above, the $v_2\{\text{EP}\}$ result without scattering is inconsistent with the measured results as a function of both $p_T$ and $\eta$. However, at $\sqrt{s_{NN}} = 19.6$ GeV, the $v_2\{\text{EP}\}$ results in all four cases are nearly consistent. This appears to indicate that, within AMPT, the $v_2\{\text{EP}\}$ measurement is dominated by nonflow contributions and does not reflect the true flow even at low $p_T$.

[1] I. Arsene *et al.* (BRAHMS Collaboration), Quark gluon plasma and color glass condensate at RHIC? The Perspective from the BRAHMS experiment, Nucl. Phys. A **757**, 1 (2005).

[2] K. Adcox *et al.* (PHENIX Collaboration), Formation of dense partonic matter in relativistic nucleus-nucleus collisions at RHIC: Experimental evaluation by the PHENIX collaboration, Nucl. Phys. A **757**, 184 (2005).

[3] B. B. Back *et al.* (PHOBOS Collaboration), The PHOBOS perspective on discoveries at RHIC, Nucl. Phys. A **757**, 28 (2005).

[4] J. Adams *et al.* (STAR Collaboration), Experimental and theoretical challenges in the search for the quark gluon plasma: The STAR Collaboration's critical assessment of the evidence from RHIC collisions, Nucl. Phys. A **757**, 102 (2005).

[5] P. Romatschke, New developments in relativistic viscous hydrodynamics, Int. J. Mod. Phys. E **19**, 1 (2010).

[6] U. Heinz and R. Snellings, Collective flow and viscosity in relativistic heavy-ion collisions, Ann. Rev. Nucl. Part. Sci. **63**, 123 (2013).

[7] G. Aad *et al.* (ATLAS Collaboration), Observation of Associated Near-Side and Away-Side Long-Range Correlations in $\sqrt{s_{NN}} =$ 5.02 TeV Proton-Lead Collisions with the ATLAS Detector, Phys. Rev. Lett. **110**, 182302 (2013).

[8] B. Abelev *et al.* (ALICE Collaboration), Long-range angular correlations on the near and away side in $p$-Pb collisions at $\sqrt{s_{NN}} = 5.02$ TeV, Phys. Lett. B **719**, 29 (2013).

[9] S. Chatrchyan *et al.* (CMS Collaboration), Observation of long-range near-side angular correlations in proton-lead collisions at the LHC, Phys. Lett. B **718**, 795 (2013).

[10] A. Adare *et al.* (PHENIX Collaboration), Quadrupole Anisotropy in Dihadron Azimuthal Correlations in Central $d + $ Au Collisions at $\sqrt{s_{NN}} = 200$ GeV, Phys. Rev. Lett. **111**, 212301 (2013).

[11] G. Aad *et al.* (ATLAS Collaboration), Measurement with the ATLAS detector of multi-particle azimuthal correlations in $p$+Pb collisions at $\sqrt{s_{NN}} = 5.02$ TeV, Phys. Lett. B **725**, 60 (2013).

[12] S. Chatrchyan *et al.* (CMS Collaboration), Multiplicity and transverse momentum dependence of two- and four-particle correlations in $p$Pb and PbPb collisions, Phys. Lett. B **724**, 213 (2013).

[13] B. Abelev *et al.* (ALICE Collaboration), Multiparticle azimuthal correlations in $p$-Pb and Pb-Pb collisions at the CERN Large Hadron Collider, Phys. Rev. C **90**, 054901 (2014).

[14] V. Khachatryan *et al.* (CMS Collaboration), Evidence for Collective Multiparticle Correlations in $p$-Pb Collisions, Phys. Rev. Lett. **115**, 012301 (2015).

[15] A. Adare *et al.* (PHENIX Collaboration), Measurement of Long-range Angular Correlation and Quadrupole Anisotropy of Pions and (anti)protons in Central $d + $ Au Collisions at $\sqrt{s_{NN}} = 200$ GeV, Phys. Rev. Lett. **114**, 192301 (2015).

[16] A. Adare *et al.* (PHENIX Collaboration), Measurements of Elliptic and Triangular Flow in High-Multiplicity $^3$He + Au Collisions at $\sqrt{s_{NN}} = 200$ GeV, Phys. Rev. Lett. **115**, 142301 (2015).

[17] C. Aidala *et al.* (PHENIX Collaboration), Measurement of long-range angular correlations and azimuthal anisotropies in high-multiplicity $p + $ Au collisions at $\sqrt{s_{NN}} = 200$ GeV, Phys. Rev. C **95**, 034910 (2017).

[18] J. L. Nagle, A. Adare, S. Beckman, T. Koblesky, J. O. Koop, D. McGlinchey, P. Romatschke, J. Carlson, J. E. Lynn, and M. McCumber, Exploiting Intrinsic Triangular Geometry in Relativistic He$^3$ + Au Collisions to Disentangle Medium Properties, Phys. Rev. Lett. **113**, 112301 (2014).

[19] G. Aad *et al.* (ATLAS Collaboration), Observation of Long-Range Elliptic Azimuthal Anisotropies in $\sqrt{s} = 13$ and 2.76 TeV $pp$ Collisions with the ATLAS Detector, Phys. Rev. Lett. **116**, 172301 (2016).

[20] V. Khachatryan *et al.* (CMS Collaboration), Observation of Long-Range Near-Side Angular Correlations in Proton-Proton Collisions at the LHC, J. High Energy Phys. 09 (2010) 091.

[21] V. Khachatryan *et al.* (CMS Collaboration), Evidence for collectivity in pp collisions at the LHC, Phys. Lett. B **765**, 193 (2017).

[22] R. D. Weller and P. Romatschke, One fluid to rule them all: Viscous hydrodynamic description of event-by-event central p+p, p+Pb and Pb+Pb collisions at $\sqrt{s} = 5.02$ TeV, Phys. Lett. B **774**, 351 (2017).

[23] Z.-W. Lin, C. M. Ko, B.-A. Li, B. Zhang, and S. Pal, A Multi-phase transport model for relativistic heavy ion collisions, Phys. Rev. C **72**, 064901 (2005).

[24] P. Bozek, A. Bzdak, and G.-L. Ma, Rapidity dependence of elliptic and triangular flow in proton-nucleus collisions from collective dynamics, Phys. Lett. B **748**, 301 (2015).

[25] J. D. Orjuela Koop, A. Adare, D. McGlinchey, and J. L. Nagle, Azimuthal anisotropy relative to the participant plane from a multiphase transport model in central $p$+Au, $d$+Au, and $^3$He+Au collisions at $\sqrt{s_{NN}} = 200$ GeV, Phys. Rev. C **92**, 054903 (2015).

[26] A. O. Velasquez, P. Christiansen, E. Chautle Flores, I. A. M. Cervantes, and G. Paic, Color Reconnection and Flow-like Patterns in $pp$ Collisions, Phys. Rev. Lett. **111**, 042001 (2013).

[27] K. Dusling and R. Venugopalan, Azimuthal Collimation of Long Range Rapidity Correlations by Strong Color Fields in High Multiplicity Hadron-Hadron Collisions, Phys. Rev. Lett. **108**, 262001 (2012).

[28] C. Aidala *et al.* (PHENIX Collaboration), Measurements of multiparticle correlations in $d + $ Au collisions at 200, 62.4, 39, and 19.6 GeV and $p + $ Au collisions at 200 GeV and implications for collective behavior, arXiv:1707.06108.

[29] K. Adcox *et al.* (PHENIX Collaboration), PHENIX detector overview, Nucl. Instrum. Methods Phys. Res., Sec. A **499**, 469 (2003).

[30] M. Allen *et al.* (PHENIX Collaboration), PHENIX inner detectors, Nucl. Instrum. Methods Phys. Res., Sec. A **499**, 549 (2003).

[31] C. Aidala *et al.* (PHENIX Collaboration), The PHENIX Forward Silicon Vertex Detector, Nucl. Instrum. Methods Phys. Res., Sec. A **755**, 44 (2014).

[32] A. Adare *et al.* (PHENIX Collaboration), Centrality categorization for $R_{p(d)+A}$ in high-energy collisions, Phys. Rev. C **90**, 034902 (2014).

[33] P. Sorensen, B. Bolliet, A. Mocsy, Y. Pandit, and N. Pruthi, The Rise and Fall of the Ridge in Heavy Ion Collisions, Phys. Lett. B **705**, 71 (2011).

[34] A. M. Poskanzer and S. A. Voloshin, Methods for analyzing anisotropic flow in relativistic nuclear collisions, Phys. Rev. C **58**, 1671 (1998).

[35] J.-Y. Ollitrault, A. M. Poskanzer, and S. A. Voloshin, Effect of flow fluctuations and nonflow on elliptic flow methods, Phys. Rev. C **80**, 014904 (2009).

[36] GEANT 3.2.1 Manual (CERN, Geneva, 1993); available at http://wwwasdoc.web.cern.ch/wwwasdoc/pdfdir/geant.pdf.5

[37] B. B. Back *et al.* (PHOBOS Collaboration), Scaling of charged particle production in $d + $ Au collisions at $\sqrt{s_{NN}} = 200$ GeV, Phys. Rev. C **72**, 031901 (2005).

[38] A. Adare *et al.* (PHENIX Collaboration), Transverse energy production and charged-particle multiplicity at midrapidity in various systems from $\sqrt{s_{NN}} = 7.7$ to 200 GeV, Phys. Rev. C **93**, 024901 (2016).

[39] J. D. O. Koop, R. Belmont, P. Yin, and J. L. Nagle, Exploring the Beam Energy Dependence of Flow-Like Signatures in Small System $d + $ Au Collisions, Phys. Rev. C **93**, 044910 (2016).

[40] P. Bozek and W. Broniowski, Collective flow in ultrarelativistic $^3$He-Au collisions, Phys. Lett. B **739**, 308 (2014).

[41] M. Habich, J. L. Nagle, and P. Romatschke, Particle spectra and HBT radii for simulated central nuclear collisions of C + C, Al + Al, Cu + Cu, Au + Au, and Pb + Pb from $\sqrt{s} = 62.4$-2760 GeV, Eur. Phys. J. C **75**, 15 (2015).

[42] P. Romatschke, Light-Heavy Ion Collisions: A window into pre-equilibrium QCD dynamics? Eur. Phys. J. C **75**, 305 (2015).

[43] J. Adam *et al.* (ALICE Collaboration), Charged-particle multiplicities in proton-proton collisions at $\sqrt{s} = 0.9$ to 8 TeV, Eur. Phys. J. C **77**, 33 (2017).